A combined experimental and DEM investigation of grain interlocking in sheared granular assemblies

Rui Lu [1], Qiang Luo [1, 2], Tengfei Wang [1, 2,*], David P. Connolly [3], Tao Xie [4]

[1] School of Civil Engineering, Southwest Jiaotong University, Chengdu 610031, China

[2] Key Laboratory of High-Speed Railway Engineering (Southwest Jiaotong University), Ministry of Education, Chengdu 610031, China

[3] School of Civil Engineering, University of Leeds, Leeds LS2 9JT, UK

[4] Department of Civil Engineering, McMaster University, Hamilton, ON, Canada

*Corresponding author. ORCID: 0000-0003-4079-0687; E-mail address: w@swjtu.edu.cn (T. Wang)

Abstract

Compacted granular material, integral to geotechnical engineering, undergoes translation, rotation, and interlocking when subject to shear displacements or external loads. The present study focuses on the interlocking of heterogeneous granular materials, a complex behavior influenced by gradation, compaction, and varying particle geometry, and has consequently received limited attention in existing research. To address this research gap, we conducted an analysis on the effect of grain interlocking on the shear resistance of granular assemblies, using a combination of laboratory testing and discrete element method (DEM). Initially, large-scale direct shear tests were conducted on gravel−sand mixes with varying degrees of compaction and normal pressure. One of the mixes also underwent subsequent shear reversal to explore the differences in grain interlocking between the two shearing processes on the shear plane. After analyzing the laboratory results, a mesoscopic scale investigation was performed by replicating the test using discrete element simulations. To facilitate this, granular particle geometries were measured using 3D laser scanning based on the physical lab tests. Subsequently, based on these scans, discrete element R-block and ball models were utilized to construct both the coarse and fine particles within the mix. Surface vibro-compaction was employed to regulate the degree of compaction. The results indicate that an increase in vertical pressure, coupled with a zero dilatancy angle, results in a rising stress ratio, indicative of grain interlocking. This interlocking exhibits a positive correlation with both the coarse content and the degree of compaction, and varies depending on the shear displacement. As interlocking progresses, the shear band, induced by particle movement, expands and is associated with reduced

particle rotation near the shear band. The study further reveals a consistent positive correlation between interlocking and the principal orientation angle of strong normal contact forces, as well as a correlation between interlocking and mobilized contacts.

Keywords: Granular material; Interlocking; Shear resistance; Direct shear; Discrete element method; Vibro-compaction

Graphical abstract
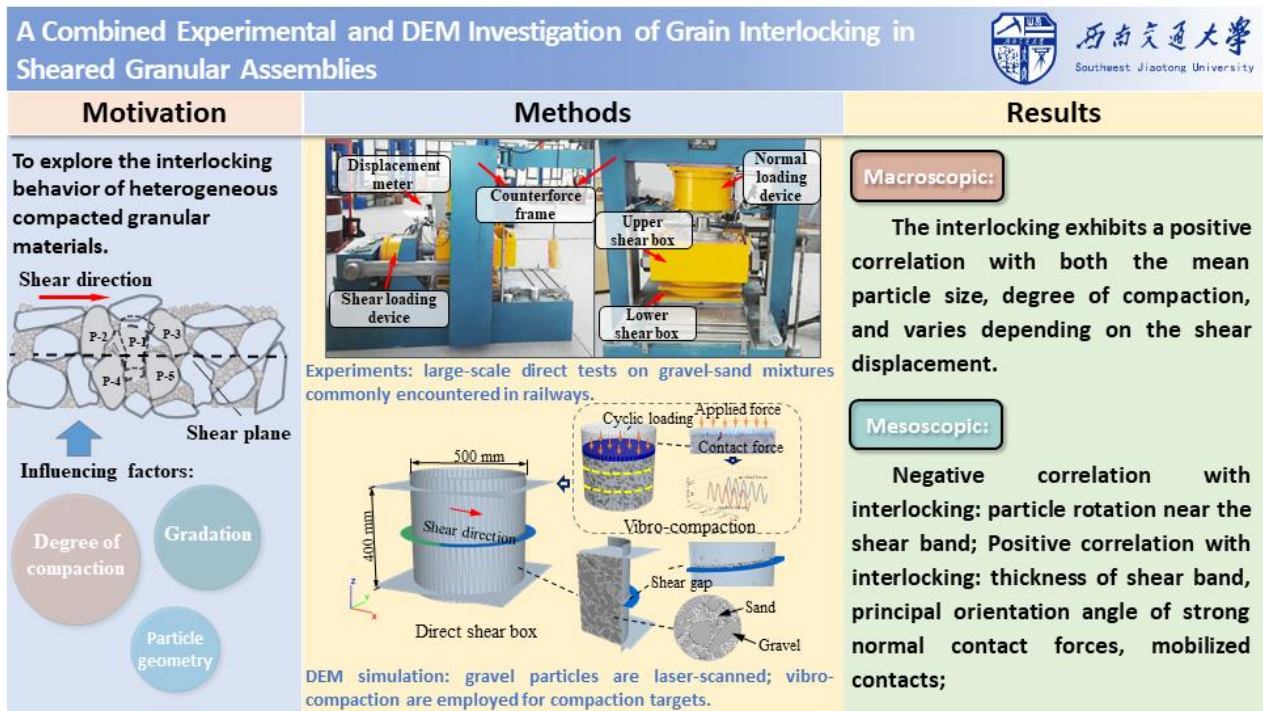
Highlights

- Investigates shear behavior in gravel−sand mixes through large-scale direct shear tests and DEM simulations.
- Explores the impact of gradation and compaction on shear stress and granular interlocking.
- Utilizes DEM to provide authentic meso-scale insights into shear resistance mechanisms.
- Identifies the role of particle size and compaction in enhancing granular interlocking.
- Reveals strain-hardening under subsequent shear reversal for different degrees of compaction.

1. Introduction

Gravel−sand mixes (GSMs) have high hydraulic permeability, favorable compaction qualities and high shear resistance (Ekici et al., 2022; Qian et al., 2020). Consequently, they have become a popular choice for high-quality fills in various engineering applications, such as railway subgrades, embankment dams, and gravel cushions (Nie et al., 2022; Xu & Wang, 2016; Zhao et al., 2016). The complexity of the genesis and internal structure of GSMs has led to their mechanical characteristics exhibiting a high degree of variability and discontinuity, which are more intricate than those of homogeneous soils or rocks (Jiang et al., 1997; Meng et al., 2018).

In soil mechanics, the resistance to shear of cohesionless soils has traditionally been attributed to inter-particle friction and dilation. It is acknowledged that the mobilized friction angle should take into account both sliding resistance and dilation due to particles rearranging and rolling over one another (Rowe, 1962; Taylor, 1948). Grain crushing also contributes to the shear resistance of non-cohesive soil, especially at high confining pressures and low void ratios (Lee and Seed, 1967). The mobilized friction angle (φ_f) is influenced by the packing arrangement of particles and the total number of sliding contacts, particularly when dilation first appears (Rowe, 1962). Typically, φ_f lies within the range $\varphi_\mu < \varphi_f < \varphi_{cv}$, where φ_μ denotes the inter-particle friction angle associated with the sliding of neighboring grains, and φ_{cv} represents the constant-volume friction angle. However, the staggered arrangement of granular materials, which affects macro-behaviour, also involves interlocking resistance (Chen, 1994; Wang et al., 2018). Guo and Su (2007) demonstrated, using Ottawa standard sand and crushed limestone, that the friction angle of granular materials is governed by four components: (1) inter-particle friction and possible crushing, (2) particle rearrangement and rotation, (3) mechanical interlocking, and (4) dilation. Therefore, distinguishing between mechanical interlocking and dilatancy is essential.

Various experimental methods, including triaxial and direct shear tests, have been employed to determine the shearing properties of sand backfills (Bareither et al., 2008a). Early studies suggested that shearing resistance increases significantly as the size of the largest particle increases (Dunn and Bora, 1972). Furthermore, Bareither et al. (2008b) devised a multivariate regression model for predicting the friction angle of compacted particles that share comparable geological origins based on maximum dry density, effective particle size, and Krumbein roundness (Krumbein, 1941). Cinicioglu and Abadkon (2015) established a connection between the dilatancy angle of cohesionless soil, relative density and mean effective stress, which enabled predictions of dilatancy angle. However, these early investigations of gravelly soils were limited to laboratory tests and focused primarily on macro-mechanical behavior. Moreover, although the resolution of X-ray micro-tomography has improved, making it possible to examine the meso-behavior of granular material (Cheng and Wang, 2018a, 2018b; Fonseca et al., 2016), it still has limitations. For instance, handling specimens with a large number of particles presents difficulties.

Alternatively, the discrete element method (DEM) has been employed to gain insight into the mechanical behavior of granules from a meso-mechanical perspective (Cundall and Strack, 1979). Interlocking is widely acknowledged as a crucial factor in soil mechanics, with researchers quantifying interlocking indirectly by examining various mesoscopic features, including friction, shape, and rotation. It has been shown that inter-particle friction plays a critical role in rearranging the contact network, resulting in discordant behaviours at the macroscopic scale (Chen et al., 2020; Zhou et al., 2021; Zhu et al., 2021). Further, (Gong et al., 2024; Nie et al., 2021b) suggested particle

shape influences meso-structural characteristics, such as coordination number and contact fabric, leading to different mechanical responses of particles. Liu et al. (2023) proposed a competition mechanism to explain the synergistic effect in the case of dilation and interlocking for granular soils with different particle shapes. They proposed a modified constitutive model that considered the impact of interlocking within the framework of the bounding surface.

To summarise, existing research has predominantly focused on the shear resistance of sand or sand-like materials. However, the mechanical behavior of GSMs under shear deformation is complex due to gradation, compaction, and particle shape. Unlike homogeneous granular materials, mixed granular matter displays significant differences in stress transmission and internal structure (Jiang et al., 2015). Consequently, there is a need for further understanding of granular interlocking. Grain interlocking, according to the Mohr-Coulomb strength criterion, contributes to both friction and apparent cohesion components of granular material shear strength (Guo, 1987; Wang et al., 2018). Given that the apparent cohesion component seems to be closely related to shear displacement, the movement of grains at the micro-scale in experiments, as well as meso-behavior by DEM, can aid in understanding the formation and variation of interlocking.

Initial large-scale direct shear tests are conducted on two typical GSM gradations commonly encountered in railways (Feng et al., 2024), with applied vertical stresses at low levels, approaching actual conditions. Subsequently, gravel particles are laser-scanned, enabling the preparation of three-dimensional DEM simulations, wherein the meso-scale parameters are calibrated through compaction targets and test results. A mesoscopic analysis of the sheared soil behavior then follows. This study aims to investigate the evolution of shear resistance corresponding with interlocked grain motion as shear displacement accumulates. Furthermore, the influence of factors including gradation, degree of compaction, and shear process by establishing correlations between the interlocking effect and meso-phenomena including particle movement, contact force, and the evolution of mobilized contacts are studied.

2. Laboratory testing

Laboratory tests were conducted with two primary objectives. The first objective aimed to discern whether grain interlocking could be analysed through macroscopic mechanical responses. The second objective sought to generate data for validating the DEM model, thereby furthering our understanding of interlocking through mesoscopic analysis. To achieve this, GSMs of varied gradation and compaction levels were prepared in accordance with technical specifications. Large direct shear experiments, which incorporated a subsequent shear reversal process, were also carried out to demonstrate the mobilization of grain interlocking as shear displacement developed.

2.1 Materials and preparation

Two types of GSMs, derived from the track beds of the Wuhan-Guangzhou high-speed railway and primarily composed of Permian hard limestone, were selected for laboratory testing. Literature (Nazir et al., 2013) indicates that the unconfined compressive strength (UCS) of limestone core samples ranges from 21.18 to 100 MPa, averaging 59.64 MPa. The Ministry of Housing and Urban-Rural Development of PRC (2014) defines rocks as hard if their

UCS exceeds 30 MPa, while the National Railway Administration of PRC (2017) categorizes them as hard when UCS surpasses 20 MPa. Thus, the soil materials used in this study are less prone to fragmentation. Fig. 1 depicts the gradation characteristics of these samples, and Table 1 summarizes their key physical properties. Classified as well-graded gravels (GW) as per the Ministry of Housing and Urban-Rural Development of PRC (2007), these materials have a specific gravity of 2.81 (Liu et al., 2023a). The maximum dry densities and optimal moisture levels were established using large-scale compaction tests per (Ministry of Water Resources of PRC, 1999). This involved a DJ30-5 electric compactor with a 35.2 kg rammer, operating at a 600 mm fall height to deliver 2688 kJ/m^3 energy. Minimum dry density was ascertained using the fixed-volume method specified by (Ministry of Water Resources of PRC, 1999), which entails methodically sliding particles into a cylinder to form the specimen.

Specimen preparation for the direct shear tests was conducted within the shear box, adhering to the specific apparatus parameters detailed in Section 2.2. According to the guidelines (National Railway Administration of PRC, 2017, 2014) the degree of compaction (DoC) for soils in different structural layers of the subgrade should be no less than 90%. Therefore, two levels of DoC, 90% and 95%, were set for each sample. The preparation involved manually compacting the samples in three layers within the shear box, while considering the optimal moisture content and the target DoC.

Fig. 1; Table 1

2.2 Apparatus and experimental design

The large-scale direct shear tests were performed according to the procedures specified in (National Railway Administration of PRC, 2010). The test apparatus shown in Fig. 2 is capable of testing a maximum grain size of 80 mm, applying a maximum shear displacement of 150 mm, and measuring to an accuracy of 0.3 mm. The circular shear box measures 504.6 mm in diameter and 400 mm in height, with a 10 mm shear gap between the upper and lower boxes that prevents stress concentration at the shear plane. The hydraulic apparatus can exert a maximum force of 700 kN in both vertical and horizontal directions. The shear rate for all conducted tests was 1.0 mm/min. Tests concluded at either the peak shear resistance (25 mm for 95% compaction specimens) or maximum horizontal displacement (50 mm for 90% compaction specimens). During the shearing process, specimens were allowed to drain through the upper and lower permeable plates situated within the shear box. Data on shear stress, vertical displacement, and horizontal displacement were collected through a data acquisition unit linked to a computer. Table 2 describes the test scheme in detail. All direct shear tests on S-2 included a 50 mm shear reversal to assess particle rearrangement and mechanical connection between particles, and their impact on shear resistance.

Given the variable shear area, which correlates with shear displacement during a direct shear process, this study introduces a corrective measure for the shear area. As depicted in Fig. 3, the shear area A_s can be calculated in relation to the shear displacement s.

$$A_s = \left[\theta_s \cdot L^2 - s \cdot (L^2 - s^2)^{\frac{1}{2}} \right] / 2 \tag{1}$$

where L denotes the diameter of shear box; θ_s has units of radians, and can be calculated by

$$\theta_s = \cos^{-1}(s/L) \tag{2}$$

Fig. 2, 3; Table 2

2.3 Analysis of stress-displacement behaviour

Fig. 4 illustrates the experimental results of shear stress τ_s (or vertical displacement h) versus shear displacement s. Overall, the vertical displacement at various vertical pressures σ_n generally exhibits a pattern of shear contraction followed by dilatancy across all test conditions, with higher vertical pressures correspond to diminished volumetric dilation. In the case of DoC=95%, the soils attain a denser state, revealing a distinct strain-softening correlation between shear resistance and vertical displacement. Conversely, at a DoC of 90%, where the soils are less compact, the strain-softening relationship weakens and occasionally shows signs of strain-hardening, as evident at vertical pressures like 600 kPa.

The stress-dilatancy relationship of a granular mass during shearing is crucial in understanding its plastic deformation and corresponding stability. In order to investigate this relationship for GSMs using direct shear tests, nonlinear curves that relate stress ratios ($R = \tau_s/\sigma_n$) to dilatancy ratios ($D = 1 - \mathrm{d}h/\mathrm{d}s$) are presented in Fig. 5. Negative values of dh/ds indicate dilation. Specimens with higher DoC exhibit both a wider range of dilatancy ratios and greater maximum stress ratios., as compared to specimens with lower DoC, for identical gradation. Similarly, more densely compacted specimens exhibit greater maximum stress ratios. This observation could suggest that the less compact specimen approaches a critical shear state later in the process, thereby compromising the particle structure near the shear plane.

The dilatancy ratio range for S-2 exhibits a wider range in the first shear compared to the subsequent shear reversal, along with a higher maximum dilatancy ratio. Conversely, there is no significant difference in the maximum stress ratio, similar to the previous stress-displacement observations. The looser specimen tends to reach a critical state of shear process towards the later stages, thereby destroying the particle structure near the shear plane, which could explain this outcome. With an increase in vertical pressure, the stress-dilatancy curves shift to the left, implying a lower dilatancy ratio due to the stress ratio. A significant increase in the corresponding stress ratio is noted as the vertical pressure increases, particularly when the dilatancy angle is zero. Hence, it is posited that there could be a grain interlocking effect in the GSMs.

Fig. 4, 5

2.4 Interlocking effect analysis

To understand the mechanism of interlocking effects in GSMs, Fig. 6 illustrates a planar arrangement of particles within the shear band. This scenario depicts five particles that were deliberately chosen to introduce the notion of an interlocked particle. Actual conditions are acknowledged to be more intricate, given the interactive restraints imposed by neighbouring grains and the diversity of grain shapes and orientations near the shear plane. Nevertheless, this model provides insight into the evolution of mechanical constraints. Particle P-1, which is traversed by a potential straight shear plane during the direct shear, is selected for the illustration. In contrast to particles P-2 and P-3, which respond more freely during direct shear, P-1 is notably restricted by P-4 and P-5. Consequently, P-1 is categorised as an interlocked particle, with P-2 and P-3 exerting less significant influence. Once the local shear plane starts to develop, P-1 is compelled to rotate over an adjacent particle (i.e., P-5), with P-4 serving as a constraint. As the shear displacement increases, P-4 is persistently pushed away by P-1, until the grain contact between them is negligible. Once it finishes overriding, P-1 is deposited with its long axis aligned parallel to the shear direction, and its motion primarily contributes to the friction component through sliding or rotation, rather than mechanical constraint. The foregoing discussion reveals that shear resistance in specimens is influenced not only by factors such as inter-particle friction and particle arrangement but also by particle interlocking (Guo and Su, 2007; Liu et al., 2023b).

To discern the mechanical interlocking effect from shear resistance in GSMs under direct shear, the test diverges from triaxial conditions with a predetermined shear plane. Particles near the shear band maintain a limit equilibrium state, supporting the analysis with the Mohr-Coulomb criterion, as shown by:

$$\tau_s = c + \sigma_n \cdot \tan \varphi \tag{3}$$

where c and φ are the apparent cohesion and friction angle.

Literature (Wang et al., 2013; Zhang and Zhang, 2007) suggests granular particles exhibit displacement-dependent shear resistance, reflected in changes in apparent cohesion (c) and friction angle (φ) with shear displacement (s). Therefore, shear resistance at any displacement comprises the transient cohesion $\bar{c}(s)$ and friction angle $\bar{\varphi}(s)$. Equation (3) then becomes:

$$\tau_s = \bar{c}(s) + \sigma_n \cdot \tan \bar{\varphi}(s) \tag{4}$$

It is important to emphasize that GSMs are unbound granular aggregates (Härtl and Ooi, 2011; Peerun et al., 2020; Tan et al., 2020). Subsequently, $\bar{c}(s)$ refers to the apparent cohesion within these mixes. Further, considering inter-particle friction, dilation, and other factors are intimately tied to σ_n, and the interlocking effect relies on soil structure and vertical stress, the interlocking effect can be quantified as the value of $\bar{c}(s)$ when σ_n equals zero. At this juncture, the particles in the mixture remain interlocked, requiring external forces for disruption. The goodness of fit of Equation (4) is shown in Fig. 7, where the majority of values exceed 0.95, except for a few points during the initial stage. These findings substantiate that both shear stress (τ_s) and normal stress (σ_n) in the GSMs' shear plane conform to the Mohr-Coulomb criterion as shear displacement evolves.

The output of Equation (4) is plotted in Fig. 8. In Figs. 8(a) and (b), the shear resistance contributed by granular interlocking reaches a peak value at low shear displacement (near s of 5 mm), followed by an abrupt decrease towards the later stages. This suggests that mechanical constraints, or grain interlocking, are not instantaneously mobilised, making the interlocking contribution to soil shear resistance a displacement-dependent variable. GSMs are subject to granular interlocking, which becomes more pronounced as compaction levels and coarse content increase. Notably, larger d_{50} specimens show a more pronounced interlocking effect under varying degrees of compaction.

In Fig. 8(c), the fluctuation in grain interlocking is comparatively minimal relative to that observed in the initial direct shear tests shown in Figs. 8(a) and (b). This occurrence can be attributed to the breakdown of mechanical constraints previously formed between grains, which have given way to particle rotation and sliding that contribute to the frictional resistance. During the subsequent shear reversal testing, numerous grains that were once interlocked have climbed over neighboring particles and assumed the role of 'free particles' on the shear plane. This observation implies that the process is irreversible, owing to changes in the soil's mesostructure during the initial shear test. It also suggests the meso-mechanism of motion among interlocked grains leads to significant variations in the shear properties.

Data from the direct shear tests conducted by Härtl and Ooi (2011) were used in Equation 4 to compute the value of $\bar{c}(s)$, as depicted in Fig. 9. These researchers observed a similar phenomenon under conditions of zero vertical stress, where particle interlocking transpired, characterized by effective cohesion. In their experiments, Härtl and Ooi (2011) employed a shear cell with a 143 mm diameter, utilizing two types of glass bead aggregates: single beads with a 6 mm diameter, and paired beads fashioned by fusing two single beads together. A typical test series for these bead types used four normal stress levels (3.1, 6.4, 12.5, and 24.2 kPa) and employed the compacted filling method.

Fig. 8 reveals that the $\bar{c}(s)$ of single glass beads remains fairly steady (less than 0.5 kPa variation), indicating a slight interlocking effect. Conversely, the $\bar{c}(s)$ of paired glass beads is significantly higher, increasing initially before decreasing with rising shear displacement. This trend arises from the shape differences between the two particle types. Paired glass beads are more likely to form interlocked particles in the packed state than single beads, leading to a stronger interlocking effect. This analysis thus lends partial support to the applicability of Equation 4.

Fig. 6-9

3. Discrete element model development

DEM stands as a vital instrument for examining the meso-mechanical behavior of particles. Coinciding with advancements in digital 3D scanning technology, the geometries of DEM particles can be accurately reconstructed to represent the internal structure of granular assemblies. This process facilitates an in-depth analysis of mechanisms leading to the formation of interlocking effects and their connection to meso-level phenomena. This section details the methodology employed to replicate previous laboratory experiments. The procedure begins with the scanning and digital reconstruction of laboratory particles, followed by the vibro-compaction placement of the sand-gravel blend,

and concludes with calibration aligned with the direct shear laboratory examinations.

3.1 Reconstruction of lab test particles

The simulation of granular materials relies on accurate particle shape representation. Zhao et al. (2023) outline three primary methods for shape depiction in granular material computational modeling: primitive-clumped, mesh-based, and analytical-surface schemes. This study employs the mesh-based method, using surface information from real particles to construct an irregular particle model, termed the rigid block module. A non-contact 3D laser scanner (Range7, KONICA MINOLTA) was utilized to obtain the surface information of coarse gravels ranging in size from 5 mm to 60 mm. However, sand particles, with diameters smaller than 5 mm, were substituted by spheres in the subsequent DEM analysis owing to the disparity in shape characterisation. To ensure statistical stability in the grains' shape characteristics, a sufficiently large number of samples were processed. According to (Ouhbi et al., 2017), when the particle count exceeds 400, the statistical properties of the grains' shape characteristics become stable. Following the approach used in (Xiao et al., 2017), 500 gravel particles were selected for scanning from the experimental set. The resulting partial scan of gravel point clouds is illustrated in Fig. 10.

Zhao et al. (2023) highlights the importance of shape in interparticle interactions. Our particle models incorporate both polyhedral and spherical particles. The Narrow-phase contact detection method is employed for interparticle contacts. For polyhedron-to-polyhedron interactions, the GJK algorithm (Gilbert et al., 1988) is utilized. In cases involving polyhedron-to-sphere contacts, we use a method inspired by Nezami et al. (2006) to locate the closest point on the polyhedral surface relative to the sphere's centroid, achieved through facet connectivity.

Fig. 11(a) presents the frequency distribution histogram of the global shape parameter, sphericity ψ ($\psi = D_i/D_c$, where D_i represents the diameter of the largest inscribed sphere and D_c is the diameter of the smallest circumscribed sphere of the particle) (Cho et al., 2006). This histogram encapsulates 500 gravels, including both real gravel particles and rigid blocks. For both real gravel particles and rigid blocks, ψ adheres to a Gaussian distribution with essentially identical probability density functions, signifying that the sphericity characteristics of natural gravels align with those of rigid blocks. A slightly higher ψ value for rigid blocks arises from the diameter of the largest corresponding inscribed sphere. According to (Lu et al., 2023, 2022), Wadell's roundness (Wadell, 1935) better represents particle angularity of rigid blocks when the facet count approximates 300. Therefore, setting rigid blocks to 300 increases the simulation accuracy in terms of angular scale. The rigid block module, representing the convex shape of real particles, has limitations in depicting concave features. Zhao and Wang (2016) utilized convexity C_X ($C_X = V/V_{CH}$, where V is the volume of the real particle and V_{CH} volume of its convex hull) to assess compactness—the degree to which a particle represents a convex hull. Fig. 11(b) illustrates the distribution of C_X distribution for 500 gravels, ranging

from 0.80 to 1.00 with an average of 0.92. This suggests a minimal presence of pronounced concave features. Therefore, employing the rigid block module for modeling irregular real particles is justified as an approximation.

Fig. 10, 11

3.2 Model development

A 3D DEM model was employed to simulate direct shear tests on GSMs, as depicted in Fig. 12. The direct shear device utilized in the numerical tests was consistent with that of the prior, larger-scale direct shear experiments. It had dimensions of 500 mm in diameter and 400 mm in height, with a 10 mm shear gap at the centre, encircled by a baffle wall of specified width to prevent particle spillage during shearing. The lower part of the shear box remained stationary, while the upper part was horizontally sheared at a specified rate of 5 mm/s, corresponding to a strain rate ($\dot{\varepsilon}$) of 0.01/s. In the case of cohesionless coarse-grain mixes, the direct shear test's lack of undrained conditions significantly reduces the impact of shear rate. Furthermore, this specific strain rate ensures quasi-static conditions. This is corroborated by the loading strain rate's minimal value, as characterized by the inertia number $I_{inertia}$ introduced by (MiDi, 2004):

$$I_{inertia} = \dot{\varepsilon} \frac{d_{50}}{\sqrt{\sigma_n/\rho}} < 10^{-3} \tag{5}$$

where ρ is the density of gravel–sand mixes. Accordingly, $I_{inertia}$ remains less than 10^{-4} during shear process.

The setting load was sustained by the upper and lower walls until the shear displacement reached either 25 mm for specimens with Doc=95% or 50 mm for specimens with Doc=90%, at which point the tests concluded.

It is worth noting that for the smallest of particle sizes, using identical particle sizes as those in the lab experiments would significantly alter efficacy. Moreover, simulating at an engineering scale may render the use of such particles impractical due to computational power limitations, as a vast number of particles would necessitate simulation (Coetzee, 2017). In coarse-grained mixes, fine particles with a grain size of less than 5 mm generally act as filling material (Guo, 1987). The replacement with 2-5 mm spheres ensures that the mechanical properties closely resemble those of the real specimen without affecting the corresponding soil structure. Thus, a uniform substitute for sand particles less than 5 mm in size was employed, consisting of spheres with a diameter between 2 and 5 mm. Particle scaling technology, doubling all particle sizes, was employed and has been widely used in DEM simulations (Kozicki et al., 2014; Lee et al., 2012). The diameter of the direct shear device is maintained at a ratio greater than 5.0 relative to the maximum particle size, thereby limiting boundary errors.

In order to achieve the densest specimens the inter-particle friction coefficient μ_p is usually set to zero in DEM via gravitational deposition and additional compression, as reported in (Abbireddy and Clayton, 2010; Gong et al., 2019b; Nie et al., 2021a). A larger μ_p reduces the likelihood of particle sliding, while a smaller μ_p facilitates easier

sliding, allowing particle positions to adjust more readily under external forces, thereby producing a denser aggregate. To attain the corresponding DoC, vibro-compaction simulations were conducted for each specimen. A range of packing densities was obtained based on the initial values of $\mu_p = 0, 0.1, ..., 1$, while other DEM contact parameters were set according to the calibration results depicted in Section 3.3. Compression was achieved via surface vibration compaction (Fig. 10), through a series of steps (depicted in Fig. 11):

(a) Balls corresponding to the actual specimens' gradation are produced;

(b) To ensure equivalency, Rblock units of the same size (d_e) as the balls are substituted in their specific spatial locations (particle size > 5 mm), and the total Rblock volume (V_R) must match the total volume (V_b) of the replaced balls;

(c) Upon achieving particle stability through gravitational deposition, a rigid load plate compacts the specimen, employing a 50 Hz vibration frequency and exerting a minimum force of 2.88 kN (18 kPa) and a maximum force of 52.88 kN (330.5 kPa) (National Railway Administration of PRC, 2010). The compaction process concludes once the specimen reaches a stable porosity;

(d) Repeat Steps *a*, *b*, and *c* until the specimen exceeds a height of 400 mm, at which point all particles above this height are removed;

(e) Use a 'measuring sphere' (Itasca Consulting Group, 2017) to calculate the DEM simulation specimen's porosity (n_s), ensuring that the difference between ns and n_e is less than 0.01. Begin the direct shear test simulation if satisfied. If not, follow the procedure in Fig. 13 by increasing μ_p and repositioning the specimen.

Fig. 12, 13

3.3 Calibration

The DEM parameters were calibrated based on the experimental data presented in Section 2.3. Given the absence of adhesion between the GSMs, the linear contact model was deemed suitable. Prior research suggests that the coefficient of friction varies between 0.37 and 0.64 for different rock textures, while the friction angle at the particle-structure contact surface is approximately 60% to 80% of the inter-particle friction angle (Han, 2012; Tiwari and Al-Adhadh, 2014). Referring to the calibration results of previous DEM simulations (Gong et al., 2019a; Li et al., 2022; Nie et al., 2022; Xu et al., 2019; Zhang et al., 2020), this study adopts a coefficient of inter-particle friction μ_g of 0.6 for the gravels, μ_s of 0.5 for the sands, and μ_w of 0.4 for the wall-particle friction. Given that the effective modulus for sands and gravels ranges from 0.64×10^8 Pa to 3.77×10^8 Pa (Liu et al., 2021), the contact effective modulus, denoted as E^*, was set at 1×10^8 Pa. The normal-to-tangential stiffness ratio (k_n/k_s) was chosen as 4/3, falling within the realistic range of 1.0 to 1.5 for granular materials (Goldenberg and Goldhirsch, 2005). Vibro-compaction, a dynamic process, differs from the quasi-static direct shear test, necessitating the inclusion of contact damping to account for specimen preparation. This damping can correlate with the coefficient of restitution (Qi et al., 2023). Two

damping types, local damping (β) and viscous damping (α_n for normal and α_t for tangential), are used in the energy dissipation process. The damping coefficients utilized in the numerical model were validated by (Zhou and Sun, 2013). Their investigation revealed that setting β to 0.05 and viscous damping (α_n and α_t) to 0.20 yields a numerical model with a restitution coefficient for granular materials of approximately 0.50, aligning closely with real granular materials.

Table 3 details the specific parameters, encompassing n_s for DEM simulation specimens post-vibro-compaction; the differences in n_e relative to the experimental specimens remained under 0.01. Fig. 14 compares direct shear simulations with experimental data, focusing on variations in shear stress and vertical displacement as they correlate with shear displacement.

Fig. 14; Table 3

4. Analysis of discrete element simulation results

4.1 Particle movement

Particle movement is crucial in shaping the macroscopic behavior of granular materials from a mesomechanical standpoint. The examination of particle displacements and rotations is essential for comprehending their association with the interlocking effect. However, computational challenges arise when analysing all particles. Therefore, we obtained mesoscopic results from the gravel in each simulated specimen. Fig. 15 shows the final shear status of the gravels' horizontal displacements and rotations for S-1 at 90% compaction. It is evident that both variables have a distinct shear band around the shear plane. Rotations are defined using the arithmetic square root of Euler angles, which consist of three angles that determine the orientation of a rigid body within a fixed coordinate system.

Fig. 16 displays the vertical profiles of horizontal displacements for all gravel specimens sheared at σ_n = 200 kPa. Each point on the graph represents a single gravel particle; the vertical axis denotes the vertical position and the horizontal axis indicates the horizontal displacement. The shear band thickness in each specimen can be inferred from its particle's horizontal displacement, which is roughly 6 to 7 times greater than d_{50}. Previous research (Desrues and Viggiani, 2004; Mokni, 1992) has suggested that as the grain size increases, the ratio of thickness to d_{50} tends to decline, ultimately reaching a constant limit value at approximately 7 for the largest grain sizes tested, as measured by particle deformation. These previous findings validate the current simulation results, although it should be noted that the DoC and shear process have a significant influence on strain localisation. For example, the thickness of the shear band in specimen S-1 is substantially greater at 95% compaction than at 90%, whereas there is no noticeable difference in the thickness of the shear band in specimen S-2. Additionally, for specimens with the same compaction level, the shear band thickness in S-2 slightly exceeds that in S-2 during the subsequent shear reversal process. These results are consistent with the interlocking effect shown in Fig. 7, which suggests that interparticle locking is the primary cause of strain localisation in the gravel-sand samples.

To quantify differences in particle rotation across various DoC and σ_n values, the rotations of particles within each 20 mm vertical range are averaged, as shown in Fig. 17. The rotation distributions for all specimens show a single peak across the vertical range, aligning with the shear surface, consistent with prior findings (Chen et al., 2021; Liu et al., 2019). In the same specimen, maximum rotation decreases as vertical pressure increases. For the same specimen at different compaction levels, the peak rotations are greater at 90% compaction than at 95% compaction. When comparing different specimens at the same DoC, the peak rotations for S-1 are less than those for S-2, while the peak rotations for S-2 are less than their results under subsequent shear reversal. For example, at 90% compaction, S-1 shows a peak rotation range of 20.64 to 25.75 for s = 25 mm, whereas at 95%, it ranges from 18.29 to 21.59; for S-2, the ranges are 25.02 to 30.68 at 90% and 23.20 to 25.06 at 95%; S-2 under subsequent shear reversal has a peak rotation range of 29.77 to 33.91 at 90% compaction and 26.80 to 27.89 at 95% compaction. The results are similar for s = 50 mm, with no further elaboration necessary. The data reveal a significant negative correlation between particle rotation and inter-particle locking; greater interlocking effects inhibit the rotational motion of particles within the specimen.

Fig. 15-17

4.2 Contact force

Granular materials transmit external loads from one boundary to another through the contact forces between particles, forming contact force networks that are key factors governing their mechanical properties (Radjai et al., 1998). Prior research (Azéma et al., 2009; Minh et al., 2014; Thornton, 2000) suggests that the normal contact force contributes more significantly to the deviatoric stress tensor than does the tangential contact force. Moreover, several researchers (Antony and Kruyt, 2009; Kruyt, 2016; Liu et al., 2020) argue that the fabric of strong contact forces dominates the entire contact system. To differentiate between strong and weak contact systems, the average magnitude of the contact force is commonly utilised. Therefore, this study centres on strong normal contact forces for quantitative analysis. It should be noted that strong normal contact forces were counted for all particles across the entire specimen.

In direct shear tests, the contact forces between particles are primarily aligned with the x-z plane. To facilitate intuitive analysis of this force distribution, we projected y-direction contact forces onto the x-z plane. This analysis used two-dimensional histograms to visually represent the spatial distribution of strong normal contact forces, with each histogram bar indicating a local average strong normal contact force $\overline{f}_n$ in that direction. According to prior work (Rothenburg and Bathurst, 1989), the distribution of normal contact forces can be modelled using a Fourier series, as follows:

$$\overline{f}_n(\theta) = \overline{f}_0[1 + a_n \cos 2(\theta - \theta_n)] \tag{6}$$

where $\overline{f}_n(\theta)$ is the local average strong normal contact force where it falls within the specified bar angles θ; θ_n and a_n are the principal orientation angle and the anisotropy of the strong normal contact forces, respectively; $\overline{f}_0$

represents the average strong normal contact of the entire specimen.

Fig. 18 depicts the transformation of the strong normal contact force distribution in polar coordinates, for S-1, S-2, and S-2, when subjected to subsequent shear reversal at σ_n of 200 kPa. Utilizing Eq. (6), Table 4 presents the regression parameters for each distribution in Fig. 18. Notably, four representative stages of shear distance (s) are selected: the initiation of shear ($s = 0$ mm), the maximum interlocking stage ($s = 5$ mm), the ultimate stage of S-1 shear ($s = 25$ mm), and that of S-2 ($s = 50$ mm). The strong normal contact force shows a positive correlation with shear resistance, increasing with s for all specimens; this relationship is further reflected in the specific value of $\overline{f_0}$. At the outset of shear ($s = 0$ mm), the strong normal contact forces are distributed in the vertical direction (i.e., θ_n is near 90° for each specimen) due to the vertical pressure exerted. However, it exhibits varying anisotropy in its distribution. At 90% compaction, a_n is higher than at 95% compaction, signifying increased DoC heightens the multi-directionality of the contact on the internal particles of the GSMs. As s increases, variations between specimens start to emerge. For a_n at 90% compaction, a trend of decreasing and then increasing can be observed, whereas it shows a consistent upward trend at 95% compaction, indicating the evolution of strong normal contact forces from vertical to horizontal. θ_n displays a tendency to align horizontally, but both S-1 and S-2 have greater θ_n at 95% compaction than at 90% compaction, while S-2 exhibits little difference caused by DoC in subsequent shear reversal process. Additionally, θ_n of S-2 is larger than that of S-2 under subsequent shear reversal considering the same s. Notably, for all specimens, θ_n rapidly shifts towards the horizontal between $s = 0$ and 5 mm, stabilising after $s > 5$ mm. This denotes a transition from an interlocking state to states of sliding, rolling, and dilation among internal particles. The same favorable mapping relationship between θ_n and the interlocking effect in Fig. 8 can also be seen.

Fig. 18; Table 4

4.3 Evolution of mobilized contacts

To investigate the properties of friction mobilisation in GSMs, the friction mobilisation index I_m is defined as per (Azéma and Radjai, 2012; Zhao and Zhou, 2017). Its weighted average, denoted as I_m^w, is computed using Equations (7) and (8).

$$I_m = |f_t|/\mu f_n \tag{7}$$

$$I_m^w = \frac{1}{n}\sum w_m I_m \tag{8}$$

where f_t and f_n represent the tangential and normal contact forces between particles, respectively. Here, μ signifies the interparticle friction coefficient, with the lesser value being used when μ (μ_g or μ_s) varies between contacting particles. Further, w_m denotes the probability distribution functions (PDF) of I_m at a specific shear displacement; n denotes the number of contacts between particles.

The upper limit of I_m is set at 1.0, in accordance with the Coulomb condition for calculating the tangential

contact force f_t. This signifies a fully mobilised contact, also referred to as a sliding contact. Smaller values of I_m imply weak contact, whereas larger values indicate strong contact.

Fig. 19 illustrates w_m of I_m for each specimen (note: S-1, S-2, and S-2 were subject to subsequent shear reversal) at different s when σ_n is 200 kPa. Specifically, since the interlocking effect mainly occurs near the shear surface, statistics are gathered for particles located within 100 mm above and below this surface. The results indicate that shear displacement has a significant impact on w_m of I_m. Further, increasing s causes w_m to decrease for weakly mobilized contacts while w_m increases within s of 5 mm for strongly mobilized contacts. This indicates when $s < 5$ mm, particle contacts intensify, and the interlocking effect is amplified; and conversely, when $s > 5$ mm, a transition occurs from interlocking to sliding contact. This behavior is more pronounced when DoC or coarse content increases, but not during subsequent shear reversal process.

Table 5 shows the variation of I_m^w with s and includes the Pearson's correlation coefficient (PCC) for I_m^w with $\bar{c}(s)$. This representation helps quantify and analyze differences in mobilized contacts between the different specimens. It shows at s of 0 mm (the initial state of the shear process), I_m^w for each specimen is approximately 1%, thus indicating uniform mobilization contacts. Throughout the entire shear process, the PCC values for S-1 at 90% and 95% compaction are 0.900 and 0.829, respectively. Further, for S-2 at 90% and 95% compaction, the values are 0.857 and 0.891, respectively, signifying $\bar{c}(s)$ has a better mapping to mobilise contacts. For samples S-2 with 90% and 95% compaction undergoing subsequent shear reversal, the corresponding PCC values are 0.021 and 0.492. These findings arise from the limited variability and irregular fluctuations in both I_m^w and $\bar{c}(s)$. Consequently, this leads to an absence of meaningful correlation between the two parameters. It may be concluded that the correlation between mobilised contacts and shear displacement partially validates Equation (4). Considering that this study focused on dense packing with DoCs at 90% and 95%, future research endeavors will extend to examining the impact of loose packing on grain interlocking. This will provide a more comprehensive understanding of granular behavior across a spectrum of compaction levels.

Fig. 19; Table 5

5. Conclusions

The shear behaviour of two GSMs, distinguished by gradation and compaction levels, is subjected to large-scale direct shear tests. The evaluation of interlocking effects on the shear plane adheres to the Mohr-Coulomb criterion. Employing laser scanning technology, 3D surface profiles were acquired for 500 gravel particles. Rblocks and DEM ball models were generated to characterize the specimens more authentically. DEM was used to simulate the corresponding specimens, and meso-scale parameters were calibrated in alignment with compaction targets and experimental findings. An analysis, encompassing both macro- and meso-scale perspectives, investigates the relationship between the interlocking effect in the GSMs and their internal strain localisation. This included studying particle displacement and rotation, normal contact force, and the evolution of mobilized contacts between particles.

The conclusions are:

(a) Regarding experimental results, the shear stress displays strain-softening behaviour at 95% compaction and strain-hardening behaviour at 90% compaction. Notably, the shear stress displays strain-hardening behavior under subsequent shear reversal for both DoCs of 0.95 and 0.9, with a lower variation in vertical displacement.

(b) Regarding stress–dilatancy analysis, the presence of grain interlocking in GSMs becomes apparent when the angle of dilation reaches 0. With an increase in vertical pressure, a corresponding rise in the stress ratio is observed, particularly in the first shear condition.

(c) For the interlocking effect, the extent to which interlocking affects the resistance of soil varies with shear displacement. A more substantial granular interlocking effect is observed in GSMs with larger coarse content and higher levels of compaction.

(d) The thickness of the shear band, in terms of particle displacement, is influenced by factors such as coarse content, degree of compaction, and the shear process; these collectively contribute to the interlocking effect. The rotations of all specimens display a single-peaked distribution across the vertical range, with maxima near the shear surface, indicating a negative correlation with the interlocking effect.

(e) As shear displacement increases, both the anisotropy and the principal orientation angle of normal contact forces become more pronounced. There exists a positive correlation between the interlocking effect and the principal orientation angle of strong normal contact forces, as well as a significant correlation with mobilized contacts.

Acknowledgements

Declaration of competing interest

The authors declare that they have no known competing financial interests or personal relationships that could have appeared to influence the work reported in this paper.

References

Abbireddy C, Clayton C. Varying initial void ratios for DEM simulations. Geotechnique 2010; 60: 497–502.

Antony S, Kruyt N. Role of interparticle friction and particle-scale elasticity in the shear-strength mechanism of three-dimensional granular media. Phys Rev E 2009; 79: 031308.

Azéma E, Radjai F. Force chains and contact network topology in sheared packings of elongated particles. Phys Rev E 2012; 85: 031303.

Azéma E, Radjai F, Saussine G. Quasistatic rheology, force transmission and fabric properties of a packing of irregular polyhedral particles. Mech Mater 2009; 41: 729–741.

Bareither CA, Benson CH, Edil TB. Comparison of shear strength of sand backfills measured in small-scale and large-scale direct shear tests. Can Geotech J 2008a; 45: 1224–1236.

Bareither CA, Edil TB, Benson CH, Mickelson DM. Geological and physical factors affecting the friction angle of compacted sands. J Geotech Geoenvironmental Eng 2008b; 134: 1476–89.

Chen H, Zhao S, Zhou X. DEM investigation of angle of repose for super-ellipsoidal particles. Particuology 2020; 50: 53–66.

Chen J, Indraratna B, Vinod JS, Ngo NT, Gao R, Liu Y. Stress-dilatancy behaviour of fouled ballast: Experiments and DEM modelling. Granul Matter 2021; 23: 1–13.

Chen X. Research on the strength of the coarse grained soil and the interlocking force. Eng Mech 1994; 11: 56–63.

Cheng Z, Wang J. A particle-tracking method for experimental investigation of kinematics of sand particles under triaxial compression. Powder Technol 2018a; 328: 436–51.

Cheng Z, Wang J. Experimental investigation of inter-particle contact evolution of sheared granular materials using X-ray micro-tomography. Soils Found 2018b; 58: 1492–510.

Cho G, Dodds J, Santamarina C. Particle shape effects on packing density, stiffness, and strength: natural and crushed sands. J Geotech Geoenviron 132 (5): 591–602. 2006.

Cinicioglu O, Abadkon A. Dilatancy and friction angles based on in situ soil conditions. J Geotech Geoenvironmental Eng 2015; 141: 06014019.

Coetzee C. Calibration of the discrete element method. Powder Technol 2017; 310: 104–42.

Cundall PA, Strack OD. A discrete numerical model for granular assemblies. Geotechnique 1979; 29: 47–65.

Desrues J, Viggiani G. Strain localization in sand: an overview of the experimental results obtained in Grenoble using stereophotogrammetry. Int J Numer Anal Methods Geomech 2004; 28: 279–321.

Dunn C, Bora P. Shear strength of untreated road base aggregates measured by variable lateral pressure triaxial cell. J Mater 1972;7.

Ekici A, Huvaj N, Akgüner C. Effects of Fines Content and Plasticity on Index Properties and Hydraulic Conductivity of Coarse-Fine Mixtures. J Mater Civ Eng 2022; 34: 04022037.

Feng G, Luo Q, Wang T, Connolly D, Liu K. Frequency Spectra Analysis of Vertical Stress in Ballasted Track Foundations: Influence of Train Configuration and Subgrade Depth. Transp Geotech 2024, 44: 101167.

Fonseca J, Nadimi S, Reyes-Aldasoro C, Coop M. Image-based investigation into the primary fabric of stress-transmitting particles in sand. Soils Found 2016; 56: 818–34.

G. Nezami E, MA Hashash Y, Zhao D, Ghaboussi J. Shortest link method for contact detection in discrete element method. Int J Numer Anal Methods Geomech 2006; 30: 783–801.

Gilbert EG, Johnson DW, Keerthi SS. A fast procedure for computing the distance between complex objects in three-dimensional space. IEEE J Robot Autom 1988; 4: 193–203.

Goldenberg C, Goldhirsch I. Friction enhances elasticity in granular solids. Nature 2005; 435: 188–91.

Gong J, Liu J, Cui L. Shear behaviors of granular mixtures of gravel-shaped coarse and spherical fine particles investigated via discrete element method. Powder Technol 2019a; 353: 178–94.

Gong J, Nie Z, Zhu Y, Liang Z, Wang X. Exploring the effects of particle shape and content of fines on the shear behavior of sand-fines mixtures via the DEM. Comput Geotech 2019b; 106: 161–76.

Gong J, Pang X, Tang Y, Liu M, Jiang J, Ou X. Effects of particle shape, physical properties and particle size distribution on the small-strain stiffness of granular materials: A DEM study. Comput Geotech 2024; 165: 105903.

Guo P, Su X. Shear strength, interparticle locking, and dilatancy of granular materials. Can Geotech J 2007; 44: 579–91.

Guo Q. Experimental study on shear strength properties of coarse-grained soil. J Hydraul Eng 1987: 59–65.

Han W. The study of frictional sliding characteristics of rocks and its influencing factors. Taiyuan University of Technology, 2012.

Härtl J, Ooi JY. Numerical investigation of particle shape and particle friction on limiting bulk friction in direct shear tests and comparison with experiments. Powder Technol 2011; 212: 231–9.

Itasca Consulting Group. PFC 6.0 Documentation. Minneapolis, Minnesota: 2017.

Jiang G-L, Tatsuoka F, Flora A, Koseki J. Inherent and stress-state-induced anisotropy in very small strain stiffness

of a sandy gravel. Geotechnique 1997; 47: 509–21.

Jiang X, Cui P, Ge Y. Effects of fines on the strength characteristics of mixtures. Eng Geol 2015; 198: 78–86.

Kozicki J, Tejchman J, Mühlhaus H. Discrete simulations of a triaxial compression test for sand by DEM. Int J Numer Anal Methods Geomech 2014; 38: 1923–52.

Krumbein WC. Measurement and geological significance of shape and roundness of sedimentary particles. J Sediment Res 1941; 11: 64–72.

Kruyt NP. On weak and strong contact force networks in granular materials. Int J Solids Struct 2016; 92: 135–40.

Lee KL, Seed HB. Drained strength characteristics of sands. J Soil Mech Found Div 1967; 93: 117–41.

Lee SJ, Hashash YM, Nezami EG. Simulation of triaxial compression tests with polyhedral discrete elements. Comput Geotech 2012; 43: 92–100.

Li R, Hu X, Chen F, Wang X, Xiong H, Wu H. A systematic framework for DEM study of realistic gravel-sand mixture from particle recognition to macro-and micro-mechanical analysis. Transp Geotech 2022; 34: 100693.

Liu H, Luo Q, El Naggar MH, Zhang L, Wang T. Centrifuge modeling of stability of embankment on soft soil improved by rigid columns. J Geotech Geoenviron 2023a, 149(9): 04023069.

Liu J, Zhou W, Ma G, Yang S, Chang X. Strong contacts, connectivity and fabric anisotropy in granular materials: a 3D perspective. Powder Technol 2020; 366: 747–60.

Liu S, Nie Z, Hu W, Gong J, Lei P. Effect of particle type on the shear behaviour of granular materials. Particuology 2021; 56: 124–31.

Liu Y, Gao R, Chen J. Exploring the influence of sphericity on the mechanical behaviors of ballast particles subjected to direct shear. Granul Matter 2019; 21: 1–17.

Liu Y, Liu X, Hu W. Competition mechanism between dilation and interlocking in granular soils: DEM simulation and constitutive modeling. Acta Geotech 2023b; 18: 149–69.

Lu R, Luo Q, Wang T, Connolly DP, Liu K, Zhao C. Discrete element modelling of the effect of aspect ratio on compaction and shear behaviour of aggregates. Comput Geotech 2023; 161: 105558.

Lu R, Luo Q, Wang T, Zhao C. Comparison of clumps and rigid blocks in three-dimensional DEM simulations: curvature-based shape characterization. Comput Geotech 2022; 151: 104991.

19

Meng Q, Wang H, Xu W, Cai M. A numerical homogenization study of the elastic property of a soil-rock mixture using random mesostructure generation. Comput Geotech 2018; 98: 48–57.

MiDi GDR. On dense granular flows. Eur Phys J E 2004; 14: 341–65.

Minh N, Cheng Y, Thornton C. Strong force networks in granular mixtures. Granul Matter 2014; 16: 69–78.

Ministry of Housing and Urban-Rural Development of PRC. Standard for engineering classification of rock mass (GB/T50218-2014). Beijing: China Planning Press; 2014.

Ministry of Housing and Urban-Rural Development of PRC. Standard for engineering classification of soil (GB/T50145-2007). Beijing: China Planning Press; 2007.

Ministry of Water Resources of PRC. Specification of soil test (SL237-1999). Beijing: China Water & Power Press; 1999.

Mokni M. Relations entre déformations en masse et déformations localisées dans les matériaux granulaires 1992.

National Railway Administration of PRC. Code for design of railway earth structure (TB10001-2016). Beijing: China Railway Publishing House; 2017.

National Railway Administration of PRC. Code for design of high speed railway (TB 10621-2014). Beijing: China Railway Publishing House; 2014.

National Railway Administration of PRC. Code for soil test of railway engineering (TB10102-2010). Beijing: China Railway Publishing House; 2010.

Nazir R, Momeni E, Armaghani DJ, Amin MM. Correlation between unconfined compressive strength and indirect tensile strength of limestone rock samples. Electron J Geotech Eng 2013; 18: 1737–46.

Nie J-Y, Cao Z-J, Li D-Q, Cui Y-F. 3D DEM insights into the effect of particle overall regularity on macro and micro mechanical behaviours of dense sands. Comput Geotech 2021a; 132: 103965.

Nie J-Y, Zhao J, Cui Y-F, Li D-Q. Correlation between grain shape and critical state characteristics of uniformly graded sands: a 3D DEM study. Acta Geotech 2021b: 1–16.

Nie Z, Qi Q, Wang X, Zhu Y. DEM investigation of strain behaviour and force chain evolution of gravel–sand mixtures subjected to cyclic loading. Particuology 2022; 68: 13–28.

Ouhbi N, Voivret C, Perrin G, Roux J-N. 3D particle shape modelling and optimization through proper orthogonal decomposition: Application to Railway Ballast. Granul Matter 2017; 19: 1–14.

Peerun M, Ong D, Choo C, Cheng W. Effect of interparticle behavior on the development of soil arching in soil-structure interaction. Tunn Undergr Space Technol 2020; 106: 103610.

Qi Q, Chen Y, Nie Z, Liu Y. Investigation of the compaction behaviour of sand-gravel mixtures via DEM: Effect of the sand particle shape under vibration loading. Comput Geotech 2023; 154: 105153.

Qian J, Yao Y, Li J, Xiao H, Luo S. Resilient properties of soil-rock mixture materials: preliminary investigation of the effect of composition and structure. Materials 2020; 13: 1658.

Radjai F, Wolf DE, Jean M, Moreau J-J. Bimodal character of stress transmission in granular packings. Phys Rev Lett 1998; 80: 61.

Rothenburg L, Bathurst R. Analytical study of induced anisotropy in idealized granular materials. Geotechnique 1989; 39: 601–14.

Rowe PW. The stress-dilatancy relation for static equilibrium of an assembly of particles in contact. Proc R Soc Lond Ser Math Phys Sci 1962; 269: 500–27.

Tan X, Hu Z, Cao M, Chen C. 3D discrete element simulation of a geotextile-encased stone column under uniaxial compression testing. Comput Geotech 2020; 126: 103769.

Taylor DW. Fundamentals of soil mechanics. vol. 66. LWW; 1948.

Thornton C. Numerical simulations of deviatoric shear deformation of granular media. Géotechnique 2000; 50: 43–53.

Tiwari B, Al-Adhadh AR. Influence of relative density on static soil–structure frictional resistance of dry and saturated sand. Geotech Geol Eng 2014; 32: 411–27.

Wadell H. Volume, shape, and roundness of quartz particles. J Geol 1935; 43: 250–80.

Wang L, Jiang H, Yang Z, Xu Y, Zhu X. Development of discontinuous deformation analysis with displacement-dependent interface shear strength. Comput Geotech 2013; 47: 91–101.

Wang XZ, Weng Y, Wang Xing, Chen W. Interlocking mechanism of calcareous soil. Rock Soil Mech 2018; 39: 3113–20.

Xiao J, Zhang D, Wei K, Luo Z. Shakedown behaviors of railway ballast under cyclic loading. Constr Build Mater 2017; 155: 1206–14.

Xu D, Tang Z, Zhang L. Interpretation of coarse effect in simple shear behavior of binary sand-gravel mixture by

DEM with authentic particle shape. Constr Build Mater 2019; 195: 292–304.

Xu W, Wang S. Meso-mechanics of soil-rock mixture with real shape of rock blocks based on 3D numerical direct shear test. Chin J Rock Mech Eng 2016; 35: 2152–60.

Zhang G, Zhang J. Stability evaluation of strain-softening slope based on Swedish slice method. Rock Soil Mech 2007; 28: 12–6.

Zhang J, Wang X, Yin Z-Y, Liang Z. DEM modeling of large-scale triaxial test of rock clasts considering realistic particle shapes and flexible membrane boundary. Eng Geol 2020; 279: 105871.

Zhao B, Wang J. 3D quantitative shape analysis on form, roundness, and compactness with μCT. Powder Technol 2016; 291: 262–75.

Zhao J, Zhao S, Luding S. The role of particle shape in computational modelling of granular matter. Nat Rev Phys 2023; 5: 505–25.

Zhao S, Zhou X. Effects of particle asphericity on the macro-and micro-mechanical behaviors of granular assemblies. Granul Matter 2017; 19: 1–18.

Zhao Y, Gao Y, Zhang Y, Wang Y. Effect of fines on the mechanical properties of composite soil stabilizer-stabilized gravel soil. Constr Build Mater 2016; 126: 701–10.

Zhou GG, Sun Q. Three-dimensional numerical study on flow regimes of dry granular flows by DEM. Powder Technol 2013; 239: 115–27.

Zhou W, Yang S, Liu J, Ma G, Qi T, Lin M. Effect of inter-particle friction on 3D accordance of stress, strain, and fabric in granular materials. Acta Geotech 2021: 1–16.

Zhu Y, Gong J, Nie Z. Shear behaviours of cohesionless mixed soils using the DEM: The influence of coarse particle shape. Particuology 2021; 55: 151–65.

Figures:
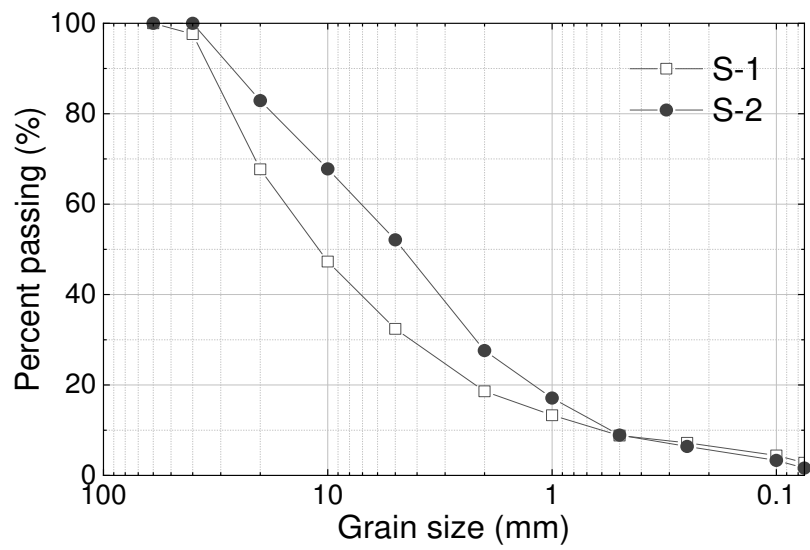
Fig. 1. Grain size distribution of the GSMs under test.
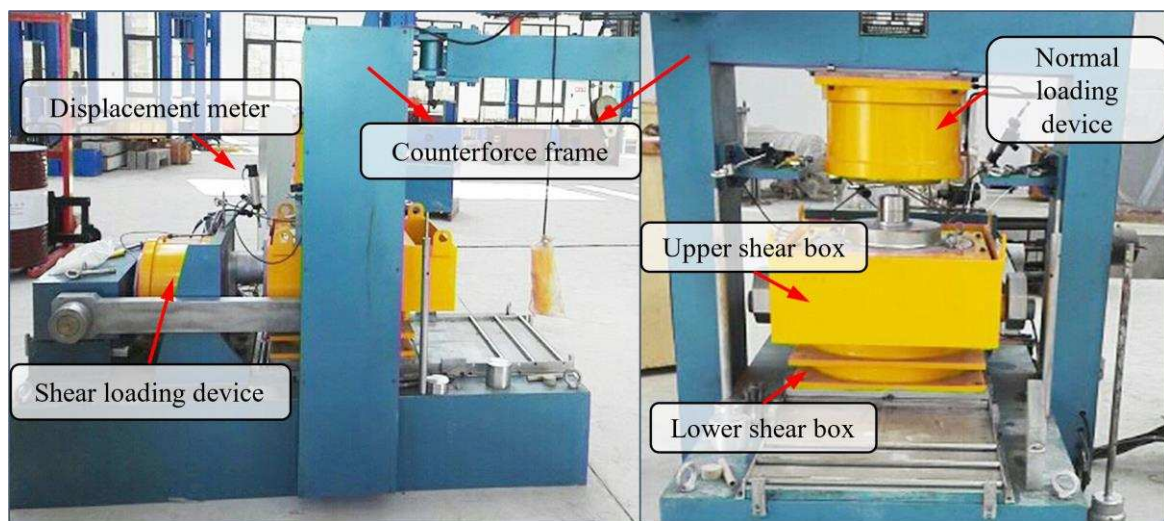
Fig. 2. Overview of the large-scale direct shear test system.
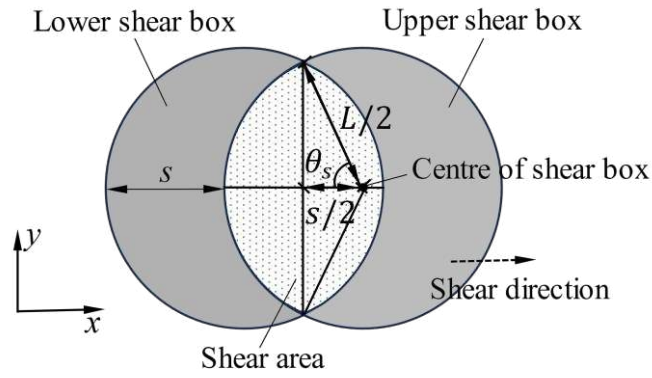
Fig. 3. Schematic of shear area correction.

(a)
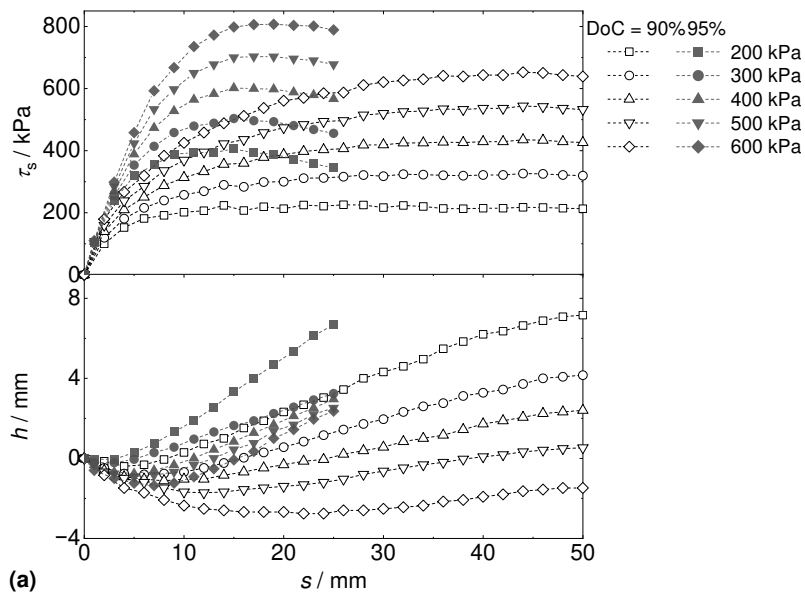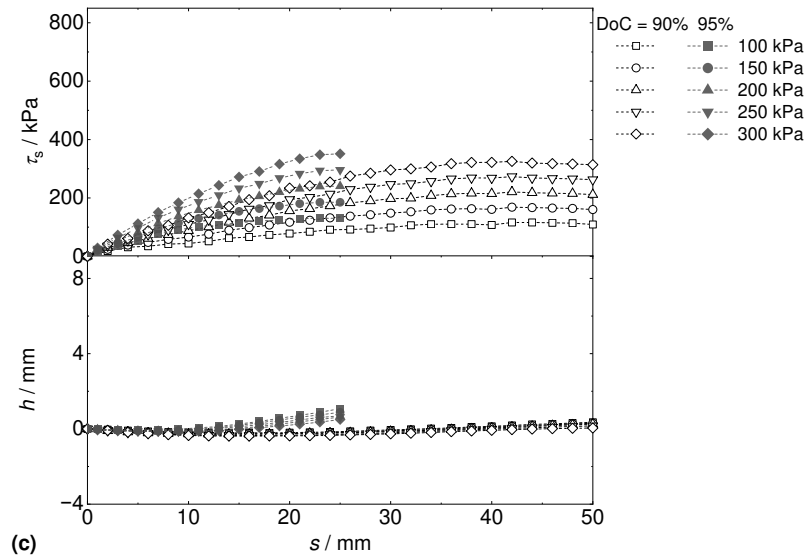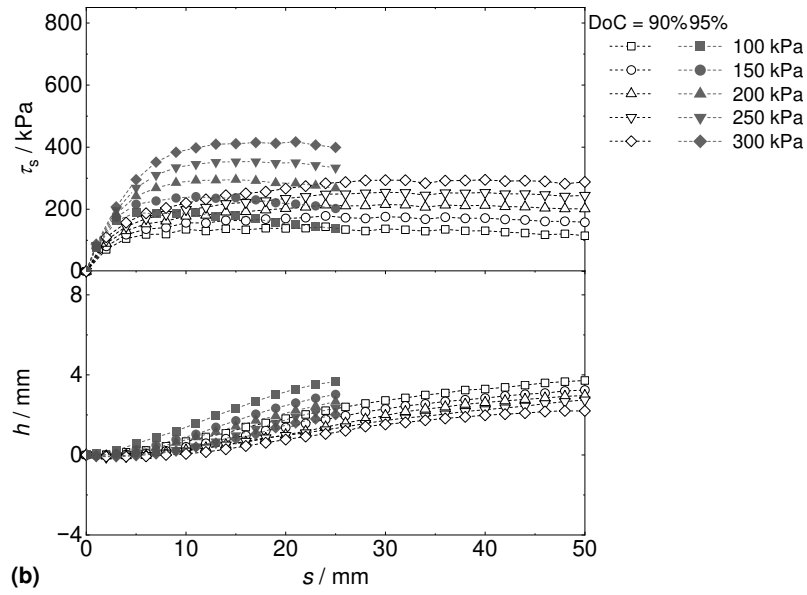
Fig. 4. Variation of shear stress and vertical displacement with shear displacement under different normal stress levels: (a) S-1; (b) initial shear of S-2; (c) S-2 under subsequent shear reversal.

[On the axis, the format for unit is *s* (mm), please revise all these figures. Thanks]
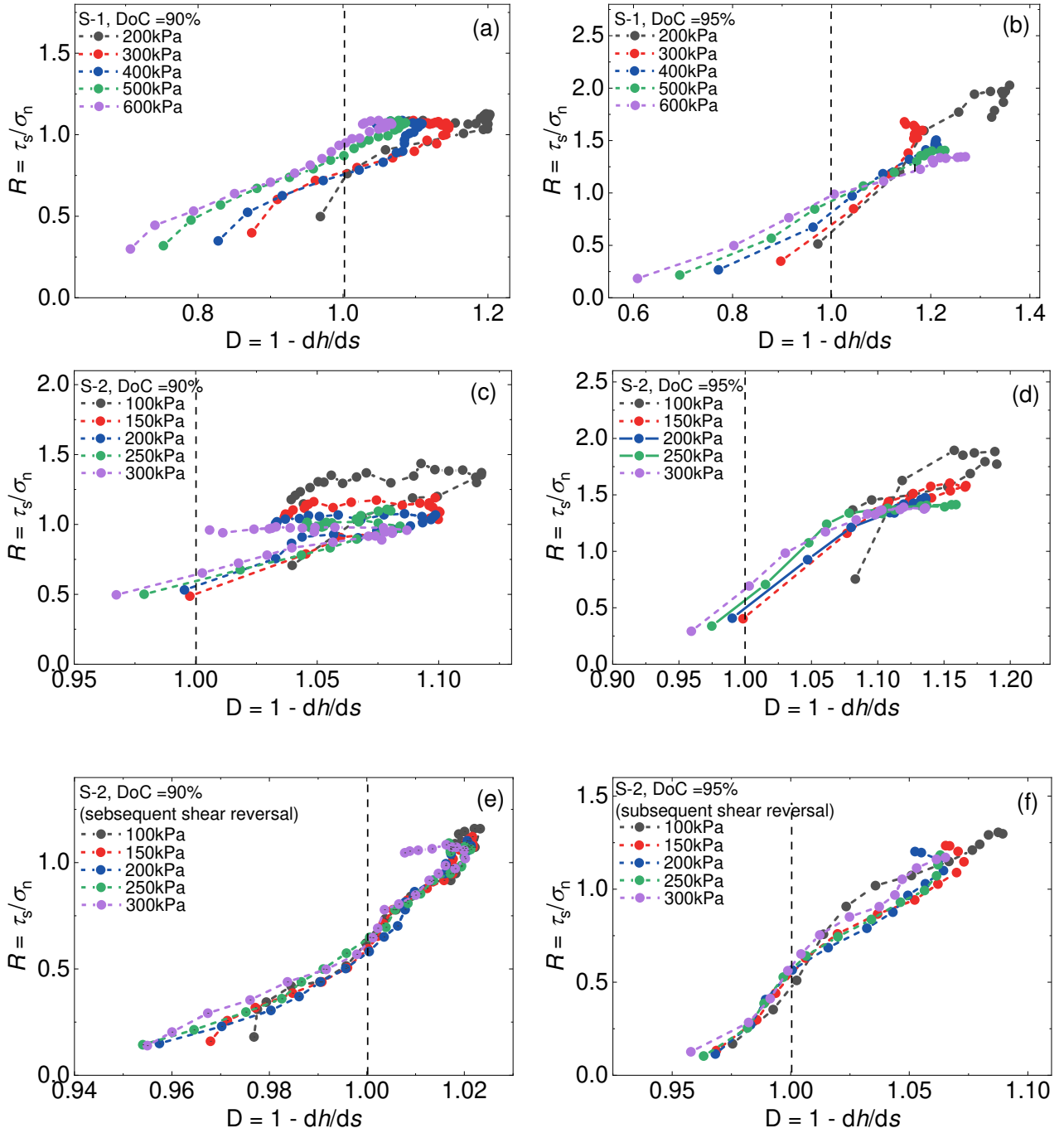
Fig. 5. Stress-dilatancy relations under various vertical stresses: (a) S-1 at 90% compaction; (b) S-1 at 95% compaction; (c) S-2 at 90% compaction; (d) S-2 at 95% compaction; (e) S-2 under subsequent shear reversal at 90% compaction; (f) S-2 under subsequent shear reversal at 95% compaction.
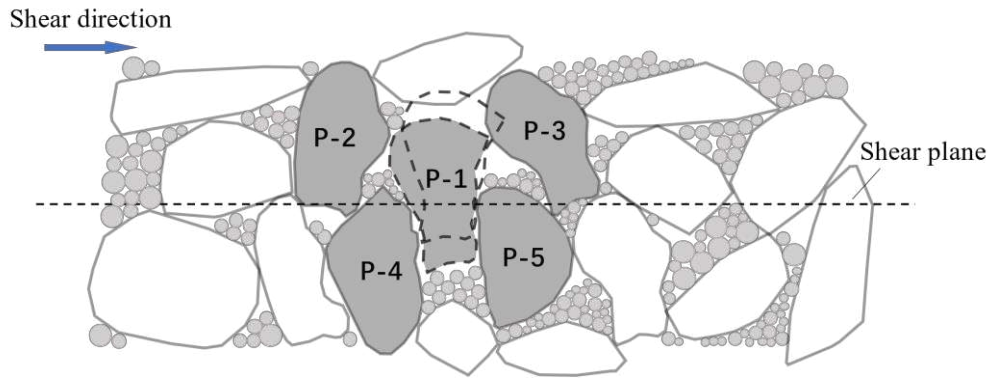
Fig. 6. Schematic of the interlocked grains in the shear plane.
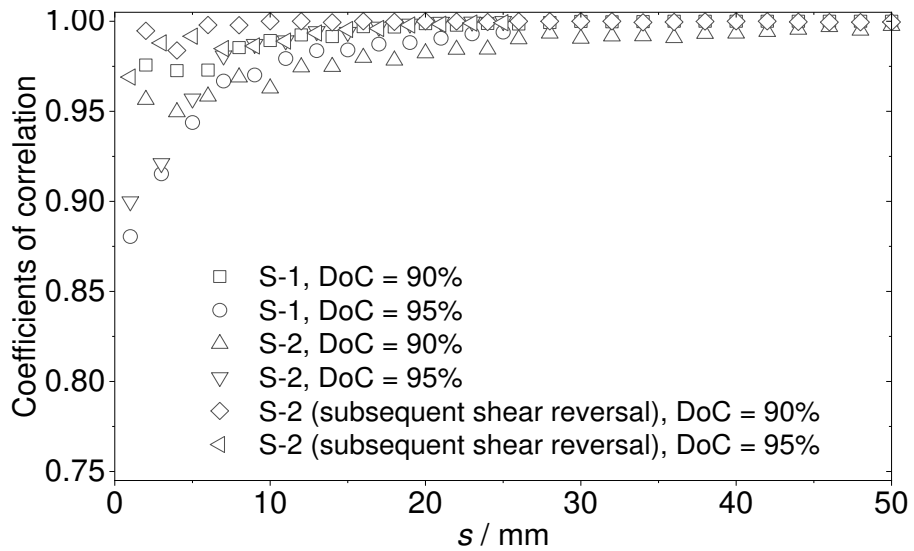
Fig. 7. Linear regression correlation coefficients between shear stress and vertical stress across various shear displacements.
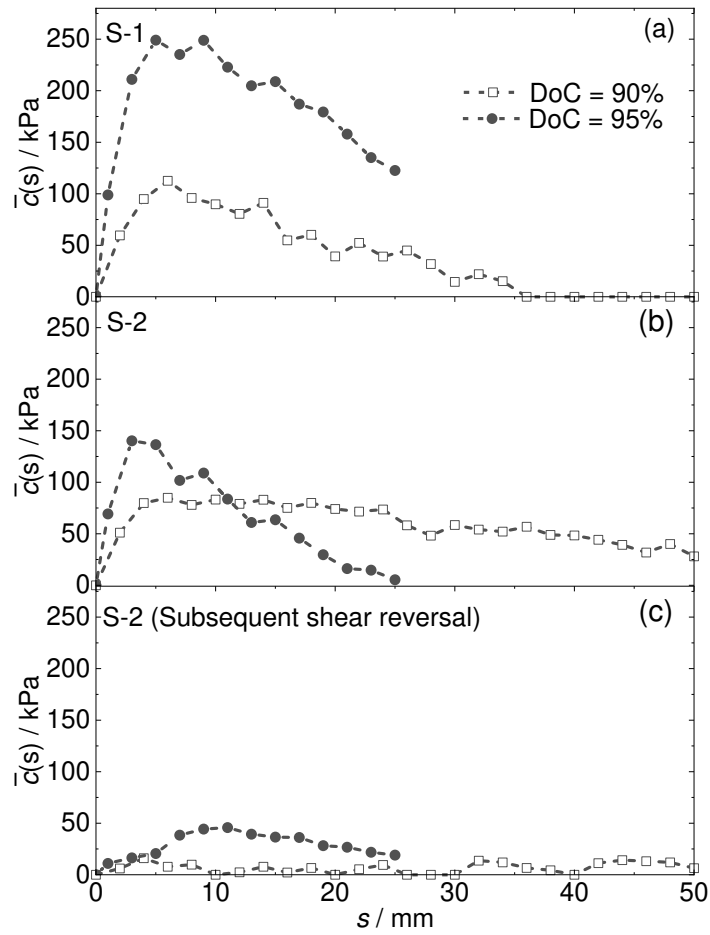
Fig. 8. Variation in grain interlocking effect with shear displacement: (a) S-1; (b) first shear of S-2; (c) S-2 under subsequent shear reversal.
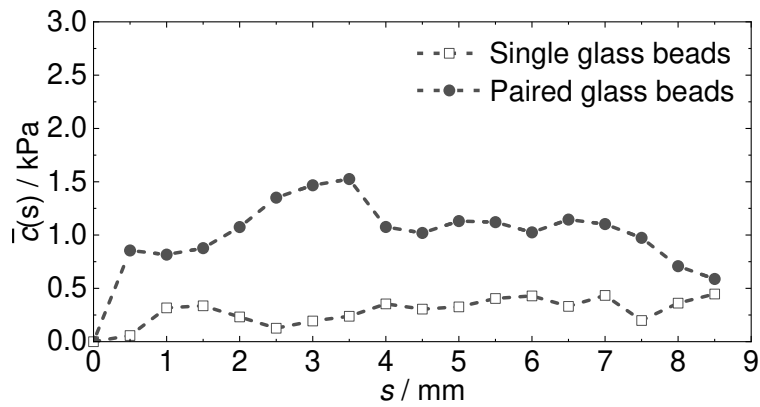
Fig. 9. Comparative analysis of interlocking effects within single and paired glass beads, based on Equation (4) and data from (Härtl and Ooi, 2011).
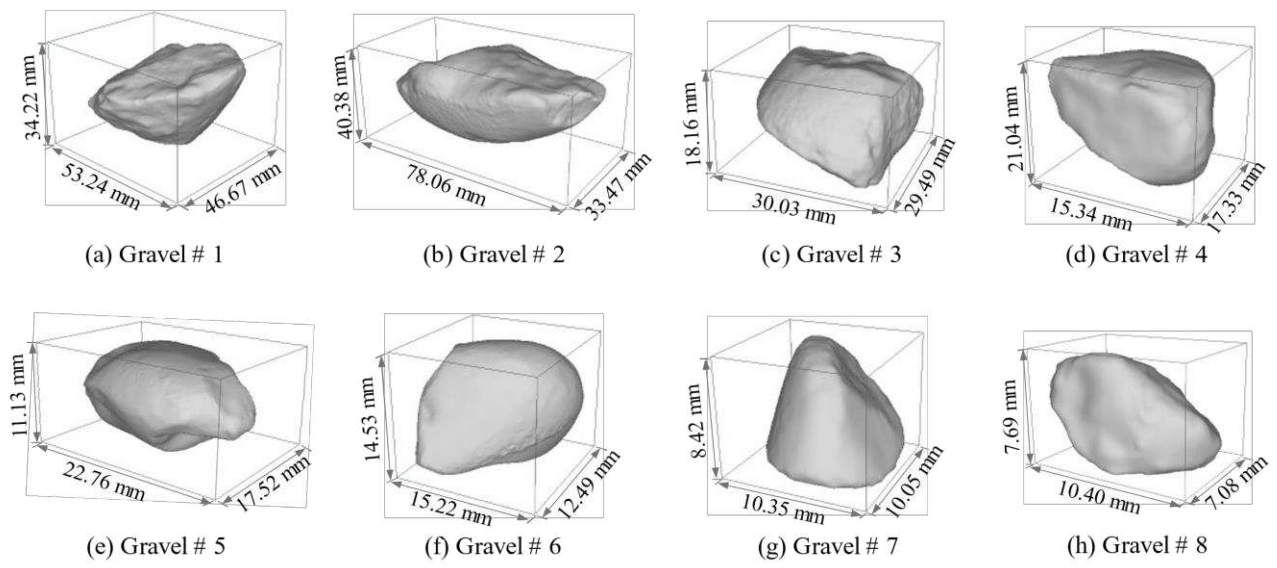
Fig. 10. Point clouds of real particles captured by laser scans.
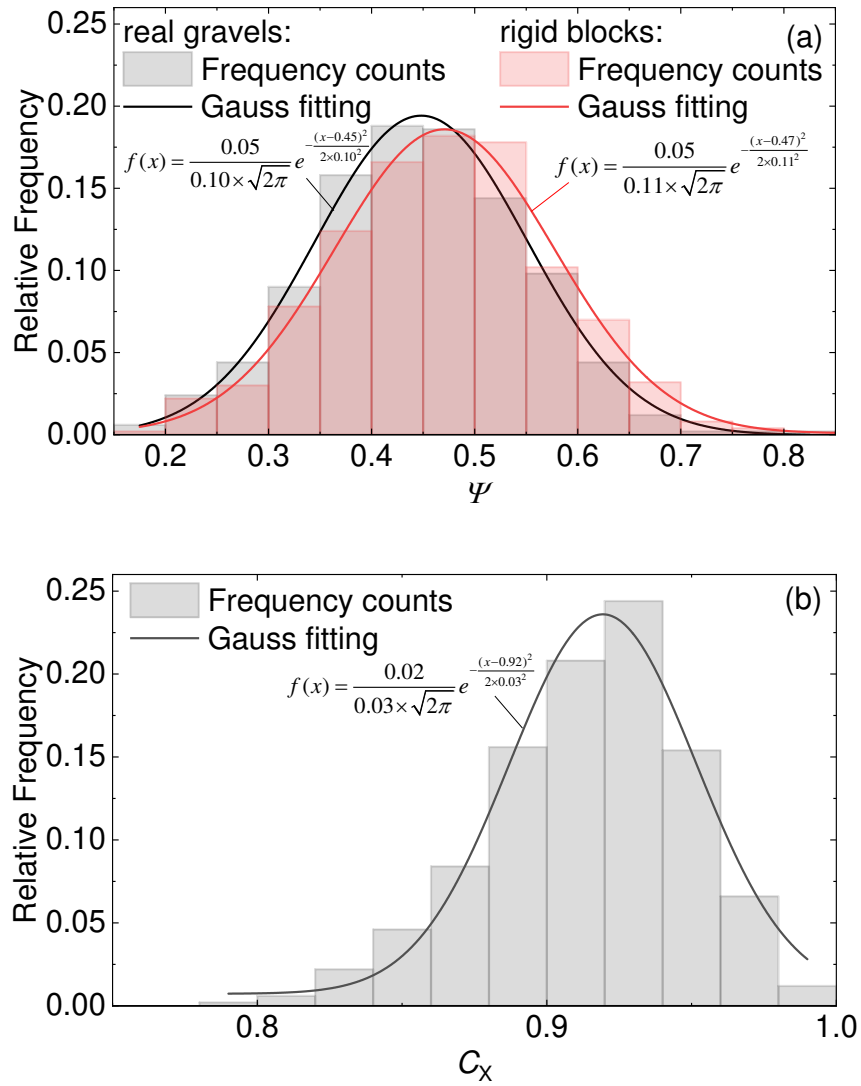
Fig. 11. Frequency histograms and probability density curve: (a) ψ for real gravels and rigid blocks; (b) C_X.
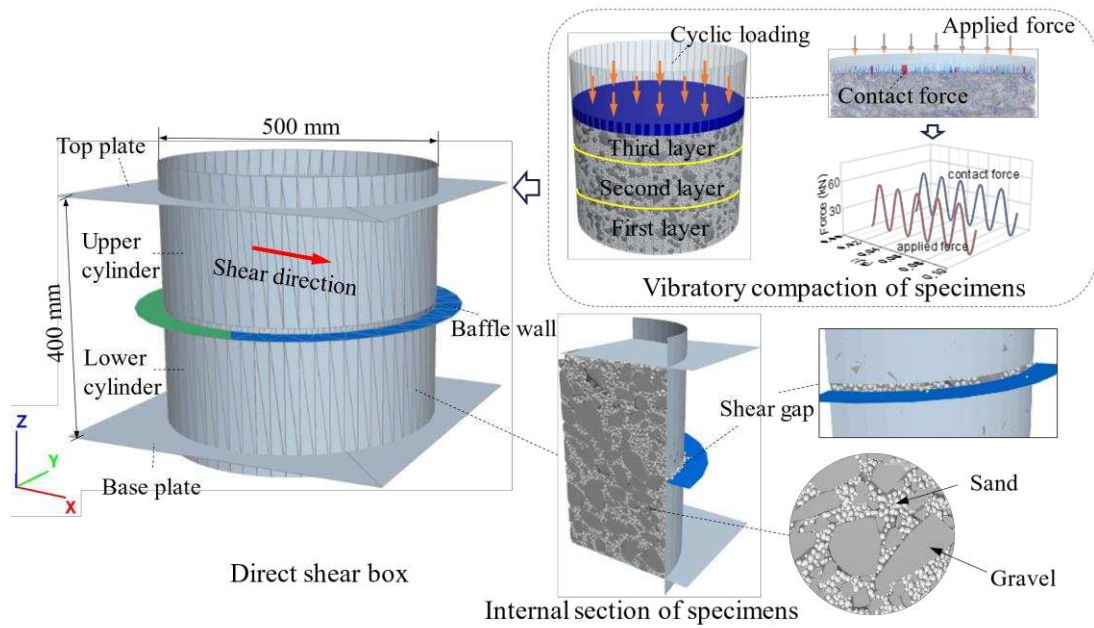
Fig. 12. Schematic of DEM simulations on direct shear tests.
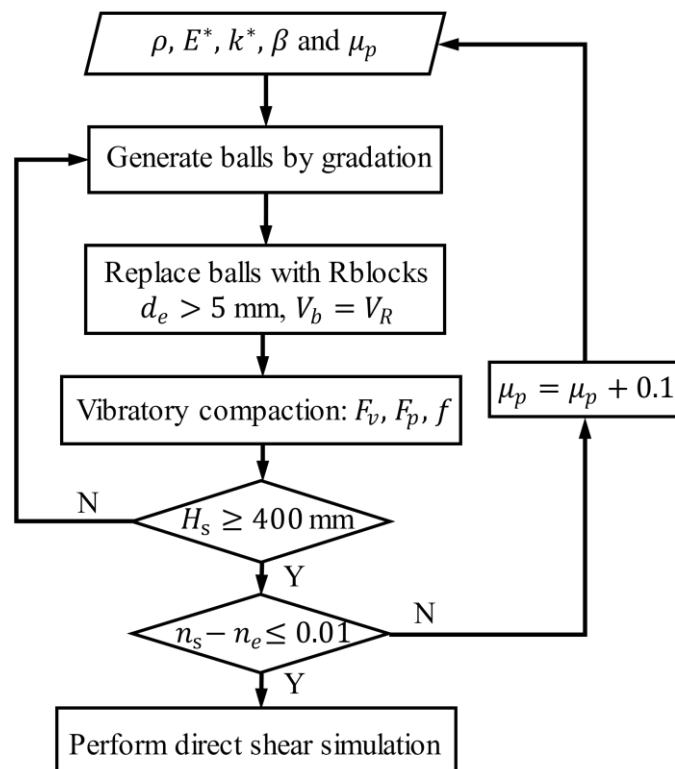
Fig. 13. Flow chart of specimen placement before direct shear tests.

(a)

(b)

(c)
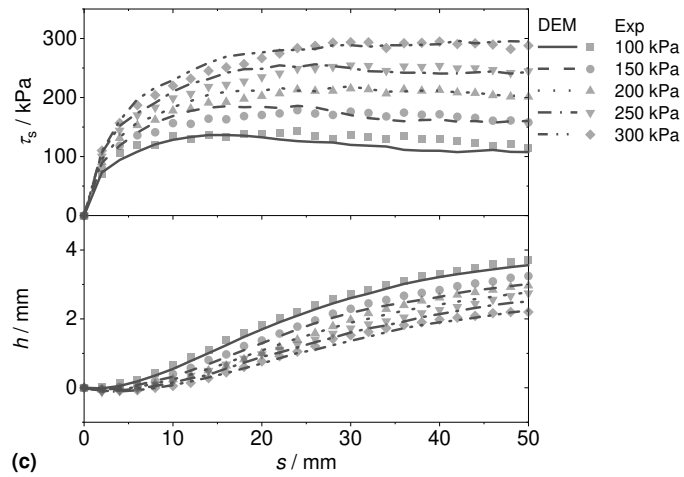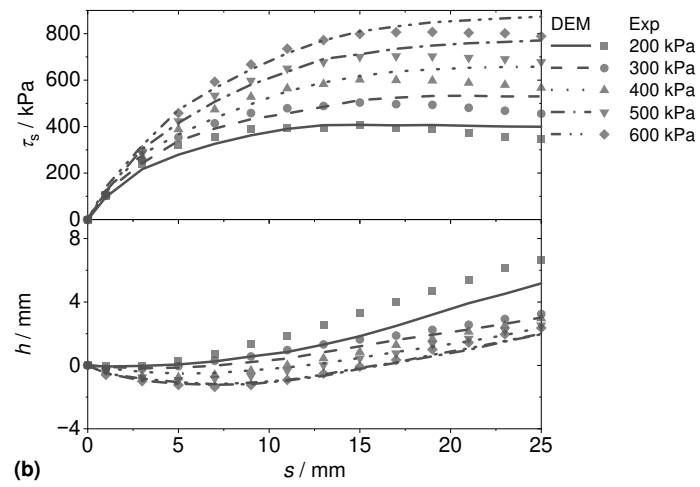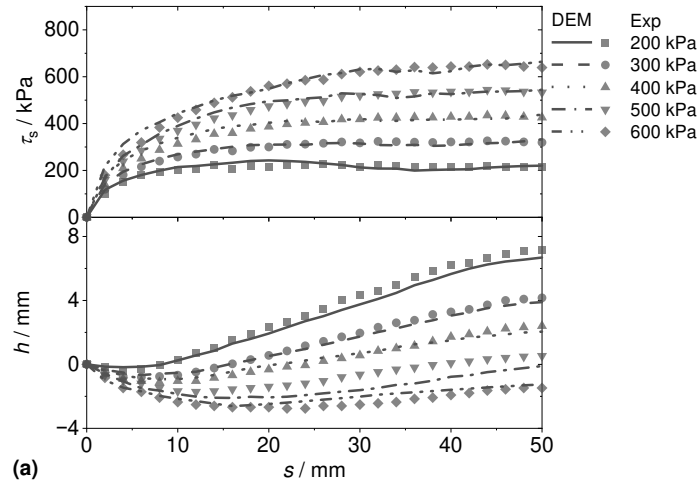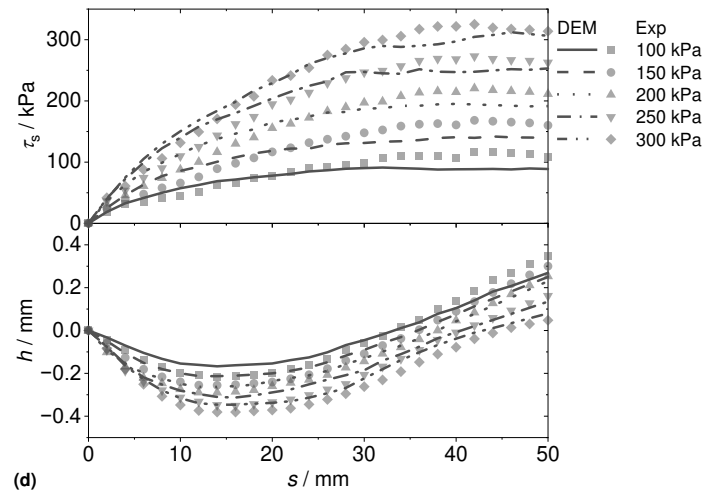
Fig. 14. Comparison of shear stress and vertical displacement curves from DEM simulations and direct shear tests: (a) S-1 at 90% compaction; (b) S-1 at 95% compaction; (c) S-2 at 90% compaction; (d) S-2 at 90% compaction following shear reversal.
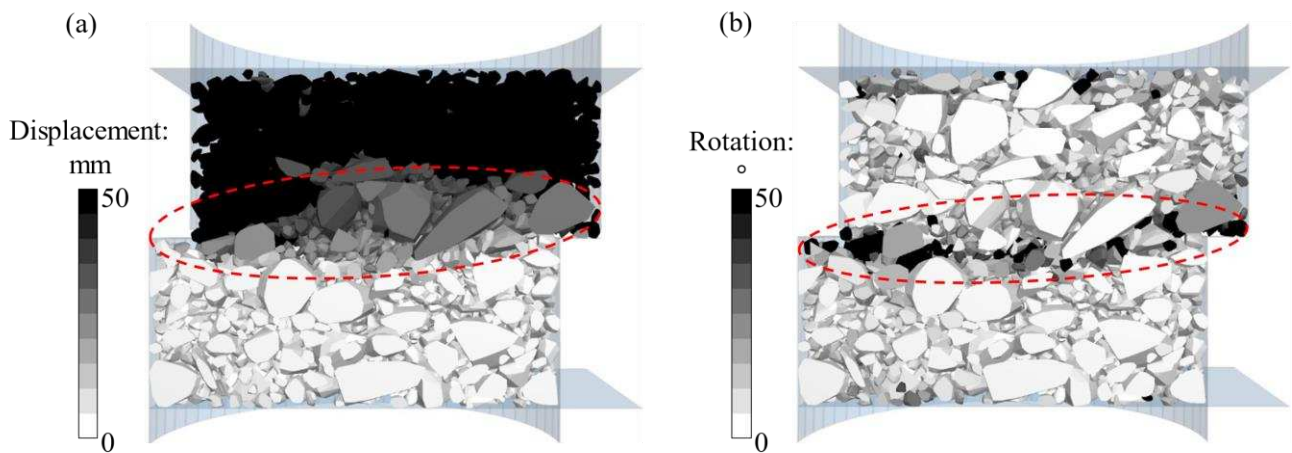
Fig. 15. Snapshots of gravel particle movement post-shearing (S-1 at 90% compaction): (a) horizontal displacement; (b) rotation.
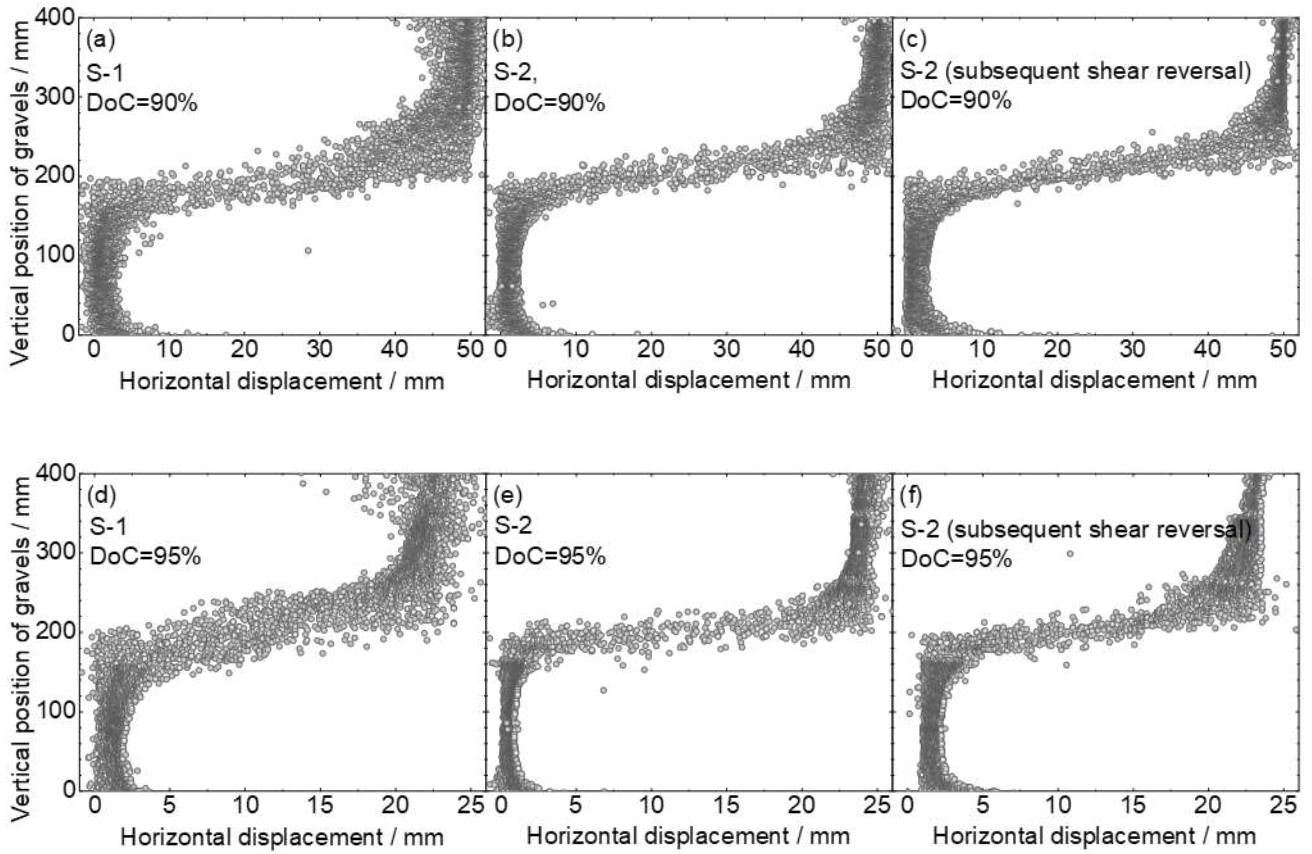
Fig. 16. Vertical profiles of gravel horizontal displacements under 200 kPa normal stress: (a) S-1 at 90% compaction; (b) S-2 at 90% compaction; (c) S-2 under subsequent shear reversal at 90% compaction; (d) S-1 at 95% compaction; (e) S-2 at 95% compaction; (f) S-2 under subsequent shear reversal at 95% compaction.
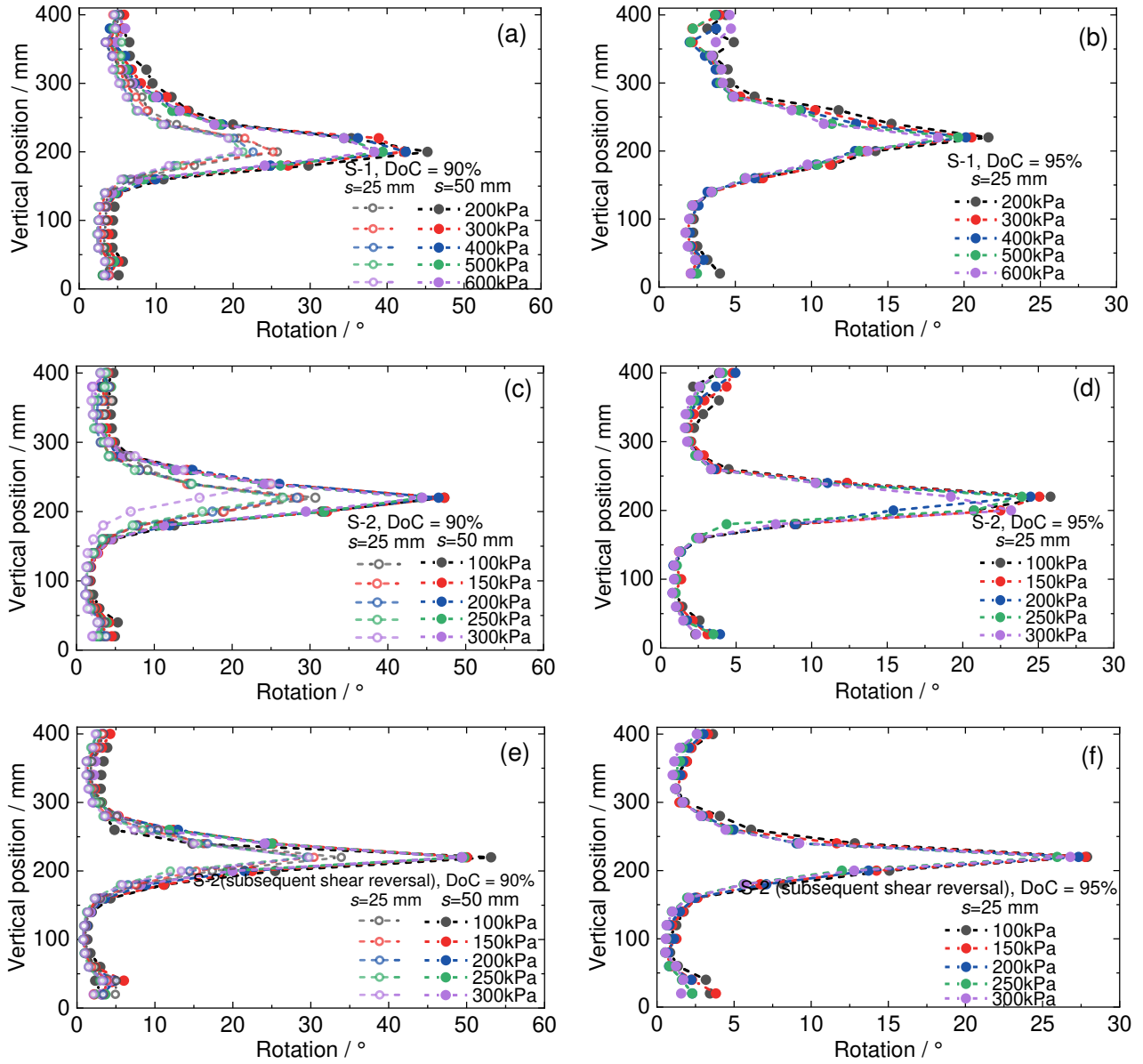
Fig. 17. Particle rotations under different normal pressures: (a) S-1 at 90% compaction; (b) S-1 at 95% compaction; (c) S-2 at 90% compaction; (d) S-2 at 95% compaction; (e) S-2 under subsequent shear reversal at 90% compaction; (f) S-2 under subsequent shear reversal at 95% compaction.
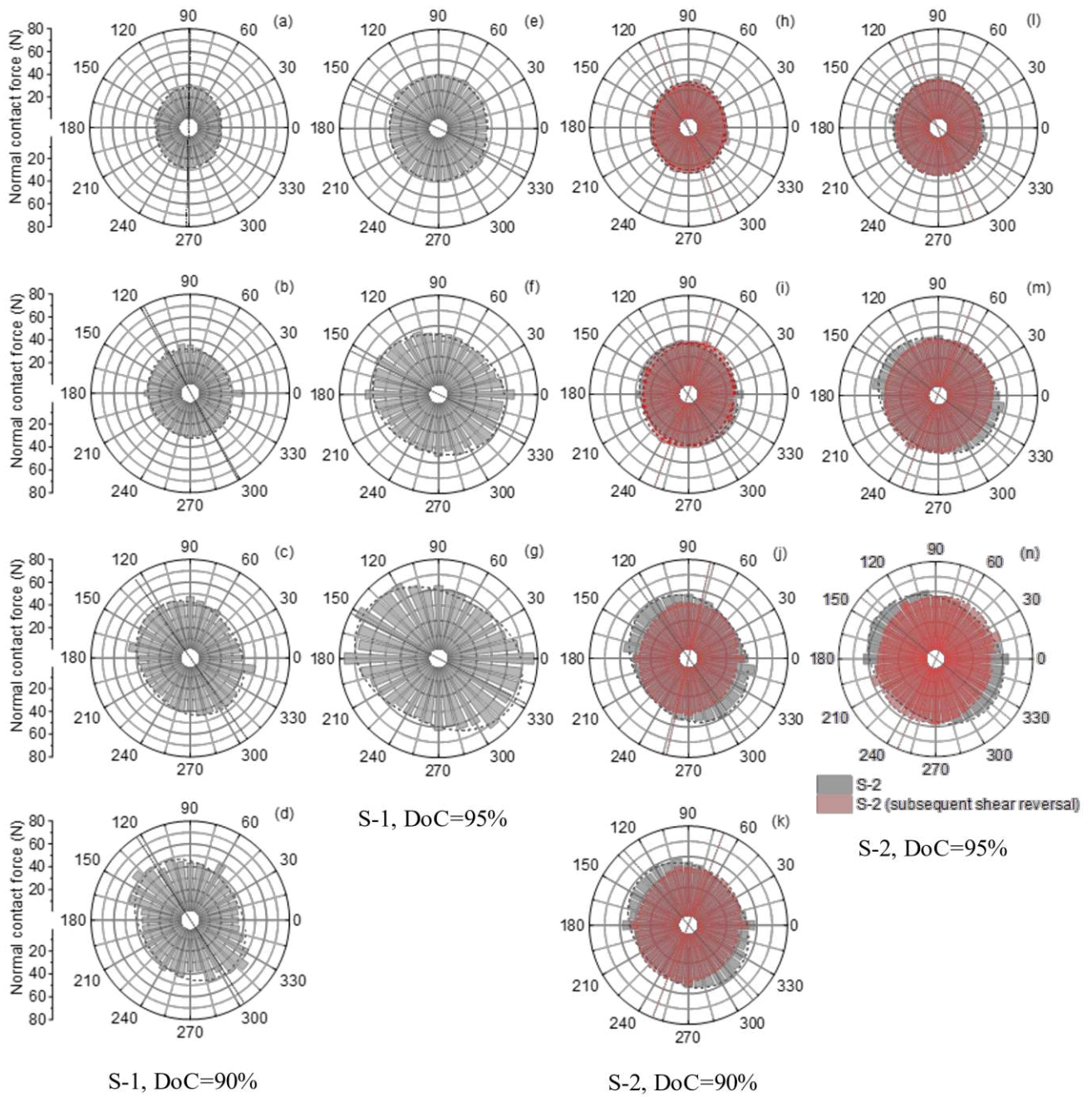
Fig. 18. Rose diagrams depicting evolution of strong normal contact forces: (a)–(d) for S-1 at 90% compaction with s of 0, 5, 25 and 50 mm; (e)–(g) for S-1 at 95% compaction with s of 0, 5 and 25 mm; (h)–(k) for S-2 (with and without subsequent shear reversal) at 90% compaction with s of 0, 5, 25 and 50 mm; (l)–(n) for S-2 (with and without subsequent shear reversal) at 95% compaction with s of 0, 5 and 25 mm.
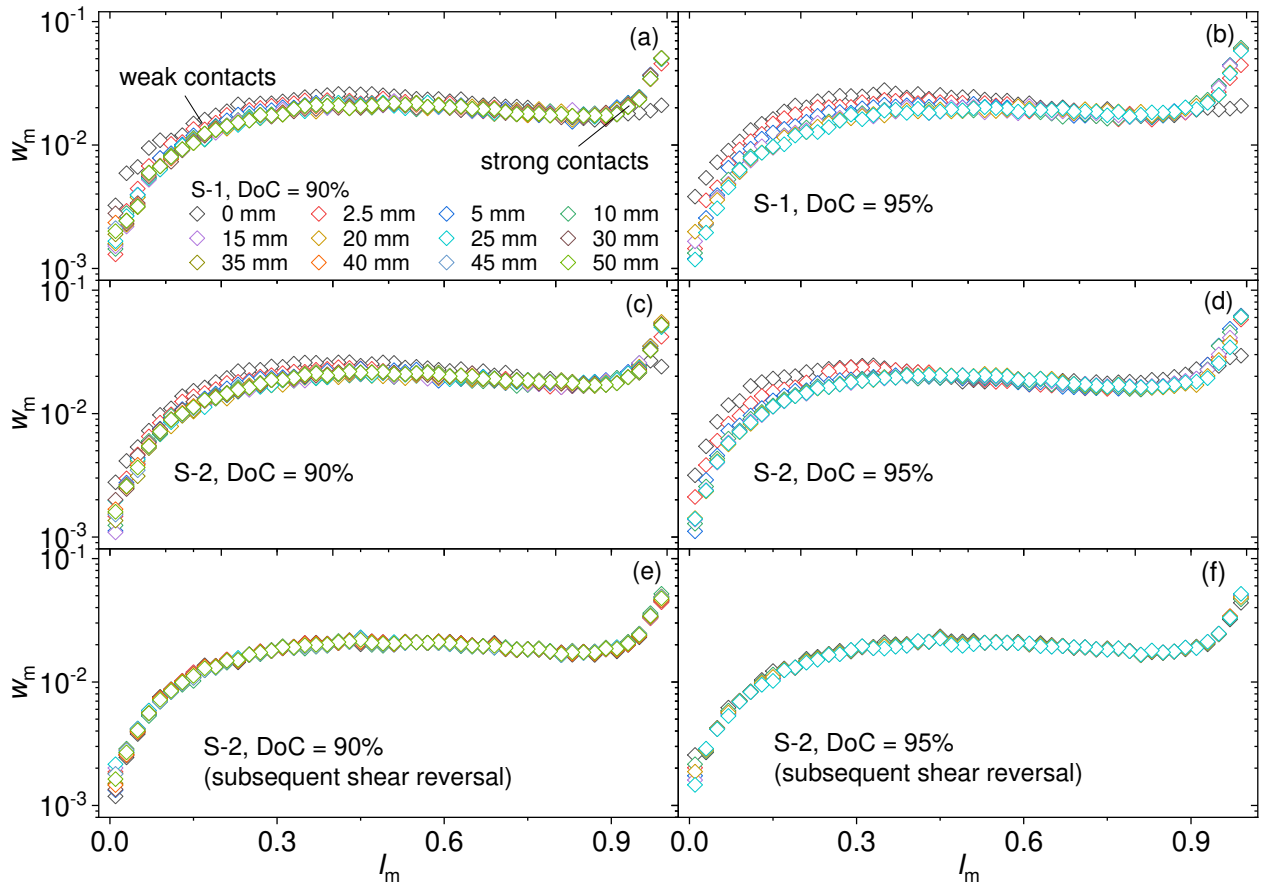
Fig. 19. Probability distribution functions (PDFs) of the friction mobilisation index I_m at various shear displacements: (a) S-1, DoC = 90%; (b) S-1, DoC = 95%; (c) S-2, DoC = 90%; (d) S-2, DoC = 95%; (e) S-2 under subsequent shear reversal, DoC = 90%; (a??) S-2 under subsequent shear reversal, DoC = 95%

Tables:

Table 1 Gradation and parameters obtained from large-scale compaction tests.

Specimen	d_{50}	C_u	C_c	ρ_{dmax} (g/cm³)	ρ_{dmin} (g/cm³)	e_{max}	e_{min}	w_{OP} (%)
S-1	11.02	24.66	1.92	2.33	1.74	0.62	0.21	5.65
S-2	4.63	13.07	1.25	2.31	1.76	0.60	0.22	4.87

Note: d_{50}: average grain size; C_u: coefficient of uniformity; C_c: coefficient of curvature; ρ_{dmax}: maximum dry densities; ρ_{dmin}: minimum dry densities; e_{max}: maximum void ratio; e_{min}: minimum void ratio; w_{OP}: optimum water content.

Table 2 Metrics for shear test on specimens.

Specimen ID	DoC (%)	D_r	n_e	Subsequent Shear Reversal (Y/N)	Normal Stress σ (kPa)
S-1	90	0.68	0.254	N	200, 300, 400, 500, 600
S-1	95	0.85	0.212	N	200, 300, 400, 500, 600
S-2	90	0.66	0.262	Y	100, 150, 200, 250, 300
S-2	95	0.84	0.221	Y	100, 150, 200, 250, 300

Note: D_r refers the relative density; n_e denotes the porosity of each specimen; "Subsequent Shear Reversal" indicates whether a follow-up shearing process was performed on the specimen after its initial shear; In cases where it is marked 'Y', the shear displacement is consistent with that of the first shear, and the shearing direction is reversed.

Table 3 Calibrated DEM parameters for direct shear simulations.

Category	Parameter description	Symbol	Value
General parameters	Particle density (kg/m^3)	ρ	2,810
	Contact effective modulus (Pa)	E^*	1×10^8
	Normal-to-tangential stiffness ratio	k_n/k_s	4/3
Friction coefficients	Wall-particle friction coefficient	μ_w	0.4
	Interparticle friction coefficient (vibro-compaction)	μ_p	0, 0.1 ···, 1.0
Damping parameters	Local damping (vibro-compaction)	β	0.05
	Normal viscous damping (vibro-compaction)	α_n	0.20
	Tangential viscous damping (vibro-compaction)	α_t	0.20
Direct shear parameters	Inter-particle friction coefficient for gravels	μ_g	0.6
	Inter-particle friction coefficient for sands	μ_s	0.5
	Local damping (direct shear)	β	0.7
Specimen properties	Porosity (S-1, DoC=90%)	n_s	0.261
	Porosity (S-1, DoC=95%)	n_s	0.215
	Porosity (S-2, DoC=90%)	n_s	0.268
	Porosity (S-2, DoC=95%)	n_s	0.225

Note: As the direct shear test is a quasi-static process, a local damping value of 0.7 is applied to the contacts, with no consideration given to viscous damping.

Table 4 Fitting parameters of Eq. (5) for each specimen.

Specimen ID	DoC	Parameter	$s = 0$ mm	$s = 5$ mm	$s = 25$ mm	$s = 50$ mm
S-1	90%	$\bar{f}_0$	25.03	30.89	40.91	42.50
		a_n	0.13	0.07	0.12	0.15
		θ_n	89.38	118.60	125.19	123.01
	95%	$\bar{f}_0$	28.30	36.00	44.44	-
		a_n	0.03	0.10	0.17	-
		θ_n	94.14	153.24	152.96	-
S-2	90%	$\bar{f}_0$	20.77	27.56	34.53	34.37
		a_n	0.11	0.07	0.13	0.13
		θ_n	91.16	128.23	125.42	129.72
	95%	$\bar{f}_0$	25.43	33.31	38.03	-
		a_n	0.03	0.10	0.13	-
		θ_n	96.83	141.86	142.04	-
S-2 (Subsequent shear reversal)	90%	$\bar{f}_0$	22.43	26.99	28.97	30.51
		a_n	0.11	0.08	0.06	0.07
		θ_n	90.93	69.90	76.95	68.12
	95%	$\bar{f}_0$	24.40	31.16	35.46	-
		a_n	0.07	0.04	0.06	-
		θ_n	91.67	69.44	66.00	-

Note: $\bar{f}_0$: average strong normal contact forces of the specimen; a_n: anisotropy of the strong contact normal force distribution; θ_n: principal orientation angle of the strong contact normal forces distribution.

Table 5. Variation of I_m^w with s and Pearson's correlation analysis for I_m^w with $\bar{c}(s)$

s	S-1				S-2				S-2 (Subsequent shear reversal)			
	DoC= 90%		DoC= 95%		DoC= 90%		DoC= 95%		DoC= 90%		DoC= 95%	
	I_m^w	$\bar{c}(s)$	I_m^w	$\bar{c}(s)$	I_m^w	$\bar{c}(s)$	I_m^w	$\bar{c}(s)$	I_m^w	$\bar{c}(s)$	I_m^w	$\bar{c}(s)$
0	1.00	0	1.01	0	1.00	0	1.00	0	1.00	0	1.01	0
2.5	1.03	59.6	1.03	211	1.02	51.1	1.03	140	1.01	6.1	1.02	16.4
5	1.04	94.9	1.07	249	1.04	84.9	1.05	137	1.01	16.1	1.02	20.6
10	1.03	89.8	1.04	223	1.03	83.2	1.04	83.7	1.02	0	1.01	45.8
15	1.02	54.8	1.03	209	1.02	75.1	1.03	63.6	1.01	2.4	1.02	36.5
20	1.02	39.2	1.03	158	1.02	74.1	1.01	16.2	1.02	7.8	1.02	26.7
25	1.01	45.0	1.02	123	1.02	58.2	1.00	5.40	1.01	0	1.02	19.1
30	1.01	14.5	/	/	1.02	58.5	/	/	1.01	9.5	/	/
35	1.01	0	/	/	1.02	56.8	/	/	1.01	0	/	/
40	1.02	0	/	/	1.02	48.4	/	/	1.01	12	/	/
45	1.01	0	/	/	1.01	31.8	/	/	1.01	0	/	/
50	1.01	0	/	/	1.01	28.1	/	/	1.01	6.4	/	/

Note: I_m^w, measured in %; $\bar{c}(s)$, measured in kPa; PCC is the Pearson correlation coefficient (S1 90%, 0.900; S1 95%, 0.829; S2 90%, 0.857; S2 95%, 0.891; S2 90% SSR, 0.021; S2 95% SSR, 0.492).